Computers & Fluids 57 (2012) 1–24

Contents lists available at SciVerse ScienceDirect

Computers & Fluids

journal homepage: www.elsevier.com/locate/compfluid

Evaluation of a rapid method for the simulation of sloshing in rectangular and octagonal containers at intermediate filling levels

Bernhard Godderidge, Stephen R. Turnock *, Mingyi Tan

Fluid-Structure Interactions Research Group, School of Engineering Sciences, University of Southampton, Highfield, Southampton SO17 1BJ, UK

ARTICLE INFO

Article history:
Received 29 April 2010
Received in revised form 20 September 2011
Accepted 22 September 2011
Available online 8 October 2011

Keywords:
Non-linear pendulum
Sloshing
Computational Fluid Dynamics
Fluid impact

ABSTRACT

The Rapid Sloshing Model methodology developed by Godderidge et al. [13], is used for the simulation of sloshing in longitudinal and transverse cross sections of membrane liquefied natural gas tanks near the critical depth. Sloshing is induced by periodic translatory and rotational tank motions at and near the first resonant period. Subsequently irregular translatory motions obtained with a realistic wave spectrum and simultaneous translatory and rotational motions are applied to the tank cross sections. The validated Computational Fluid Dynamics (CFDs) methodology from Godderidge et al. (2009) is applied and it is found that the results from the Rapid Sloshing Model are typically within 5–10% of the corresponding CFD solution for linear, weakly nonlinear and strongly nonlinear sloshing with sloshing impacts. Simulation times are typically 0.1% of real time on a desktop PC. A similar level of agreement between Rapid Sloshing Model and CFD solution is observed when an irregular motion profile from a realistic seaway is applied to the tank for a duration corresponding to 35 min on a liquefied natural gas carrier. Compared to an existing phenomenological modelling approach the RSM methodology reduces the error by up to an order of magnitude in sloshing scenarios of practical interest.

1. Introduction

Design optimisation or the use of a numerical wave tank to gather statistical sloshing data [14] require sloshing simulations with long duration. The full assessment of loading times for offshore LNG (approximately 12–18 h) with CFD is not feasible with currently available computational resources and methods. Recent incidents of sloshing damage onboard LNG carriers [17] have added further urgency to the improvement of sloshing analysis in LNG carrier and floating LNG design. Membrane containment systems are considered to be at greater risk from sloshing damage than spherical tanks and detailed sloshing studies are required to determine the sloshing characteristics of a new tank design or vessel operating profile [22]. Although a tank will experience motions in all six degrees of freedom, the most severe cases are roll, pitch, sway and surge [22] and the largest sloshing loads tend to occur at filling level – tank length ratios (filling ratios) of $0.1 \leqslant h/L \leqslant 0.5$ [23]. The initial CFD analysis is normally undertaken by considering two dimensional sloshing motions of the longitudinal and transverse cross sections of the tank [22].

This approach is adopted for the current sloshing investigation, where the sloshing characteristics of the longitudinal and transverse cross sections with a filling ratio of 0.3 and 0.4 respectively are investigated using the pendulum sloshing model introduced in part one of this two part series [13]. One full field simulation of translatory sloshing is carried for each tank shape using CFD with an excitation period at 1.25 times the first resonant period T_1 to determine the imbalance force characteristics and the remaining coefficients are obtained from theoretical results. The pendulum sloshing model is then applied to a sloshing case study outlined in Section 2 which includes a wide range of excitation motion profiles. The corresponding cases are simulated independently with the multiphase CFD sloshing model by Godderidge et al. [11] which is summarised in Section 3. The sloshing case study results for the sloshing model and the CFD simulation are compared in the time domain and frequency domain in Section 4. The resulting conclusions and ongoing further work are outlined in Section 5.

The governing equations for the rapid pendulum sloshing model introduced in Godderidge et al. [13] with simultaneous rotational and translatory excitation can be written as

$$\begin{aligned}\dot{\theta}_1 &= \theta_2 \\ \dot{\theta}_2 &= -\delta_3\dot{\theta}_1^3 - \delta\dot{\theta}_1 + \frac{1}{I}\left[gy\sin(\theta_1) + gx\cos(\theta_1)\right] \\ &\quad - \left[a\left(\frac{\theta}{\theta_{crit}}\right)^b + c\left(\frac{\theta}{\theta_{crit}}\right)^{2d}\dot{\theta}_1^m\right] + F_{Rot},\end{aligned} \tag{1}$$

with

$$gx = g\sin(\chi) + A\cos(\chi), \tag{2}$$

* Corresponding author.
E-mail address: srt@soton.ac.uk (S.R. Turnock).

0045-7930
doi:10.1016/j.compfluid.2011.09.010

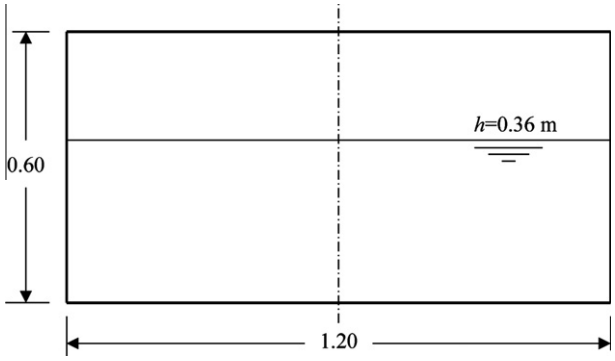

Fig. 1. Longitudinal membrane tank cross-section (all dimensions in m).

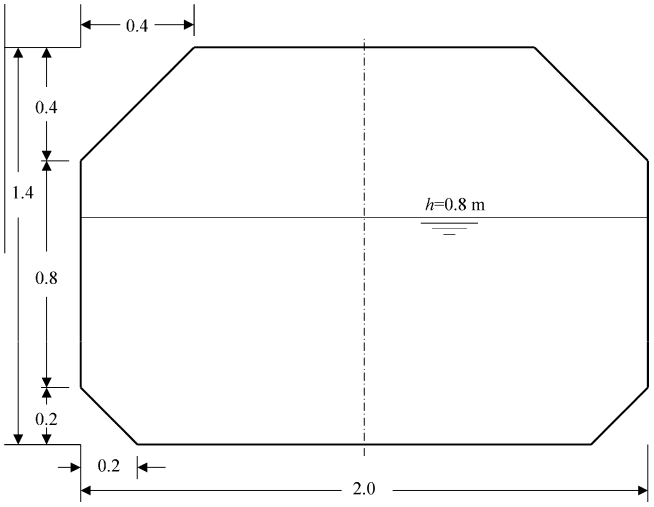

Fig. 2. Transverse membrane tank cross-section (all dimensions in m).

Table 1
Properties of the longitudinal and transverse sections.

	Longitudinal	Transverse
Filling ratio h/L	0.3	0.4
First resonant period T_1 (s)	1.474	1.736
Effective sloshing mass fraction m_1/m_{tot}	0.63	0.59

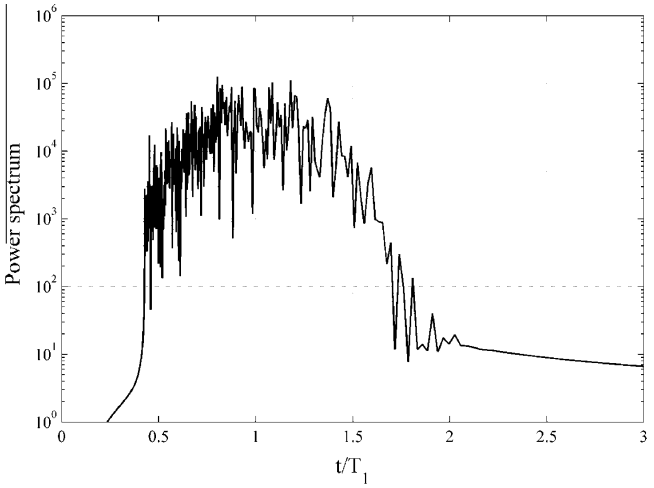

Fig. 3. Power spectrum of tank acceleration profile.

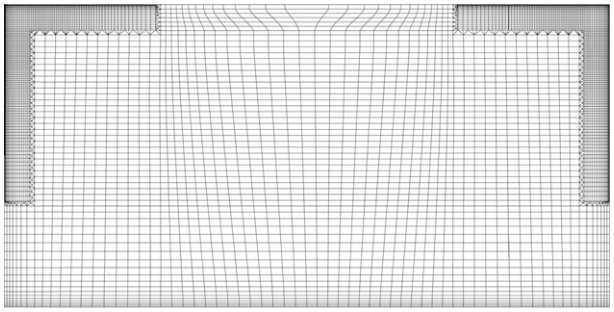

Fig. 4. Computational mesh for the longitudinal tank cross-section.

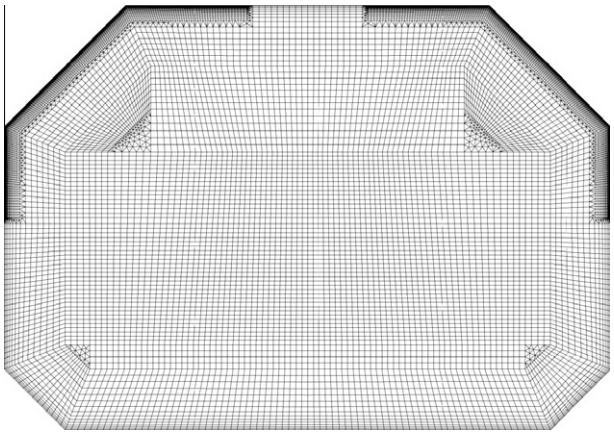

Fig. 5. Computational mesh for the transverse tank cross-section.

Table 2
Results of the grid independence study (from [9]).

Nodes	Difference relative to the finest grid (%)		
	P4	P6	P9
5600	4.83	4.29	0.72
12,000	1.44	1.45	0.44

and

$$gy = -g\cos(\chi)R(\theta_1) + A\sin(\chi), \tag{3}$$

where A is the translatory acceleration, χ the angular displacement, δ a damping coefficient, g gravity, l pendulum length and θ angular displacement. The coefficients a, b, c and d describe the damping model, θ_{crit} is the centre of mass displacement angle at which impact occurs and F_{Rot} inertial forces accounting for the rotating frame of reference. Time derivatives are indicated by superscript dots. Heave motions can be included with the introduction of a time-varying component in g. Eq. (1) is solved numerically using an adaptive Adams–Bashforth–Moulton scheme with user-specified error tolerances implemented in the software package MATLAB.

A systematic study of sloshing with increasingly realistic motion profiles is carried out. The first stage uses periodic excitations for translatory motions in cross sections representing longitudinal and transverse LNG membrane containment systems. The excitation periods vary from $0.8T_1$ to $1.1T_1$ for the longitudinal case and the larges response is observed at resonance. The range of excitation periods for the transverse cross section is reduced to the range between $0.95T_1$ and $1.05T_1$ where the most significant sloshing response is expected. The transverse cross section is then subjected to rotational motions with a range of excitation periods between $0.95T_1$ and $1.25T_1$. The third stage considers an irregular

Table 3
CFD model description and parameters.

Water	Incompressible fluid
Air	Ideal gas
Sloshing motion	Body force (translation) and rotating frame 7of reference (rotation)
Turbulence model	Standard k-ε with scalable wall function
Spatial discretisation	Gradient-dependent first or second order
Temporal discretisation	Second order backward Euler
Timestep control	$C_{N,RMS} \leqslant 0.15$
Convergence control	RMS residual $<10^{-5}$

Table 4
Rapid Sloshing Model settings for longitudinal cross section.

Length	0.5397
Effective mass fraction	0.63
Linear damping coefficient	0.024
Third-order damping coefficient	0.044
Restoring force: function	$\alpha_1\theta + \alpha_2\lvert\theta\rvert\theta + \alpha_3\theta^3$
Restoring force: coefficients	$\alpha_1 = 1.0428$
	$\alpha_2 = -0.0583$
	$\alpha_3 = -0.1272$
Impact model:	16°
Impact model: force coefficients	$a = 0.025$
	$b = 15$
Impact model: damping coefficients	$c = 0.0005$
	$a = 24$

motion profile which is obtained with an ITTC wave spectrum and LNG carrier RAOs and variations in the motion amplitude and tank height are considered. The final stage of the systematic study uses simultaneous translatory and rotational motions where the translatory and rotational periods are not necessarily coincident.

2. Sloshing investigation

2.1. Tank cross-sections

The longitudinal cross section for surge and pitch motions, shown in Fig. 1, is sized to coincide with the experiments carried out by Hinatsu [16]. Fig. 2 shows the transverse cross section of a typical membrane LNG tank with a scale factor of approximately 1:20 and it is used for the simulation of sway and roll motions. In the first two stages of the sloshing case study, the excitation motions are periodic with the tank displacement x given as

$$x = x_0 \sin(\omega t), \tag{4}$$

where x_0 is the motion amplitude, $\omega = \frac{2\pi}{T}$ excitation frequency and t time. The filling levels are 60% of tank height in the longitudinal cross section and 57% of the tank height for the transverse cross-section. This corresponds to a filling ratio h/L of 0.3 for the longitudinal cross section compared to the critical filling ratio of 0.3368.

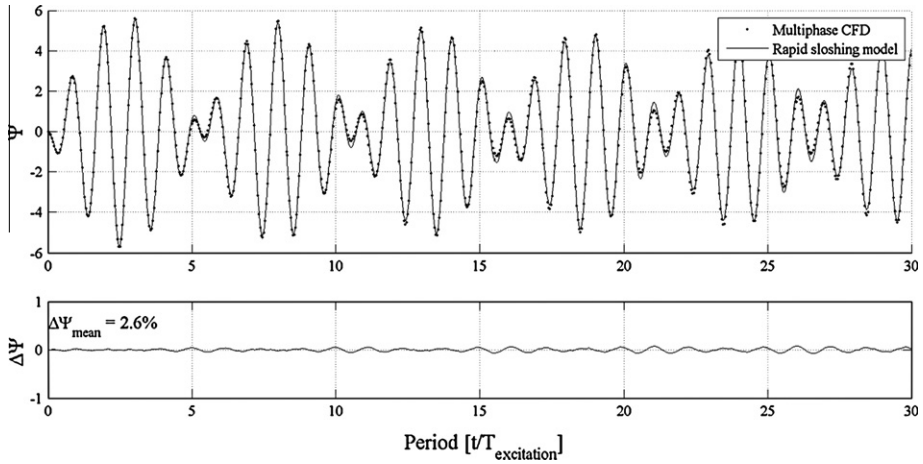

Fig. 6. Comparison of normalised fluid momentum Ψ for surge with excitation period $T = 0.80T_1$.

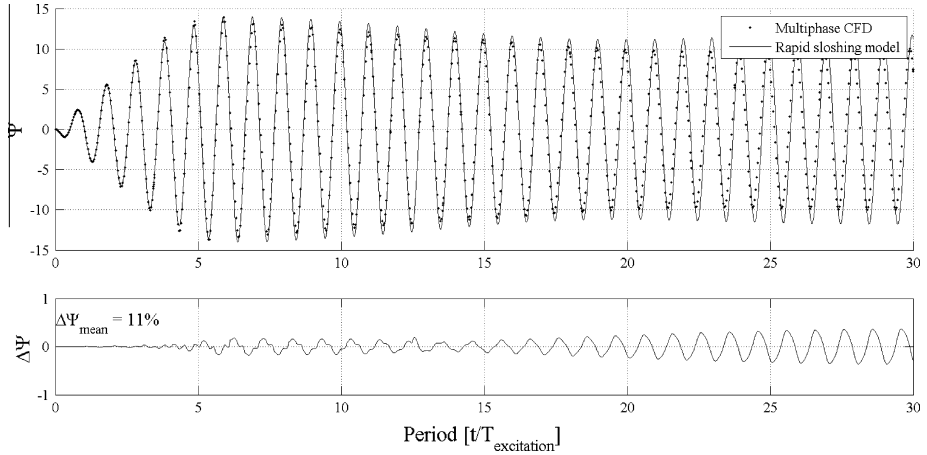

Fig. 7. Comparison of normalised fluid momentum Ψ for surge with excitation period $T = 0.95T_1$.

The resonant sloshing periods of a rectangular tank can be calculated using potential flow [1]

$$T_m = \frac{2\pi}{\sqrt{gk\tanh(kh)}}, \tag{5}$$

where g is gravity, h the filling depth and, for a two dimensional tank

$$k^2 = \pi^2\left(\frac{m^2}{L^2}\right), \tag{6}$$

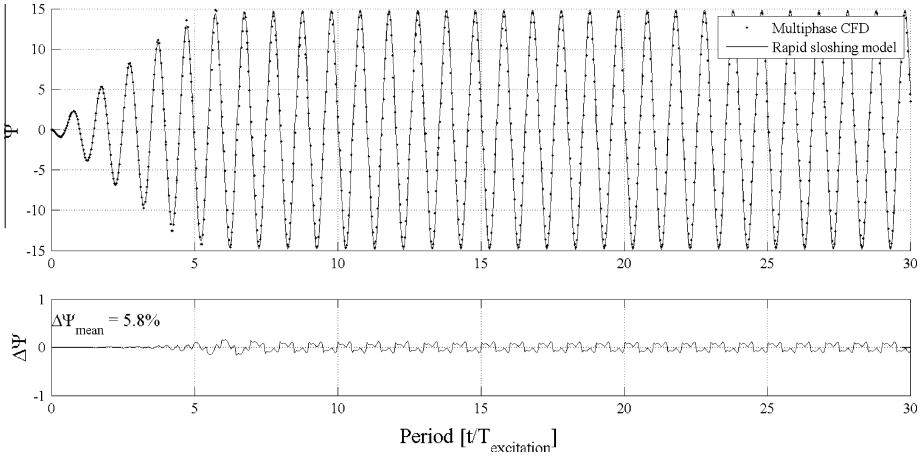

Fig. 8. Comparison of normalised fluid momentum Ψ for surge with excitation period $T = 1.00T_1$.

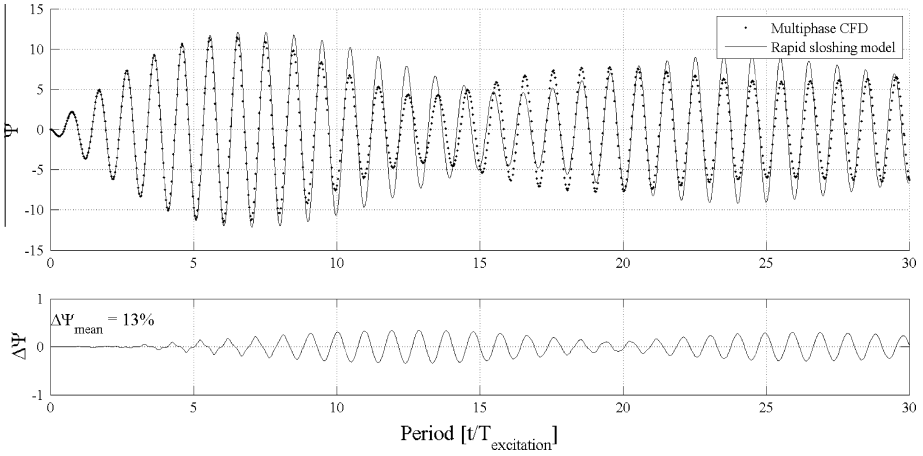

Fig. 9. Comparison of normalised fluid momentum Ψ for surge with excitation period $T = 1.05T_1$.

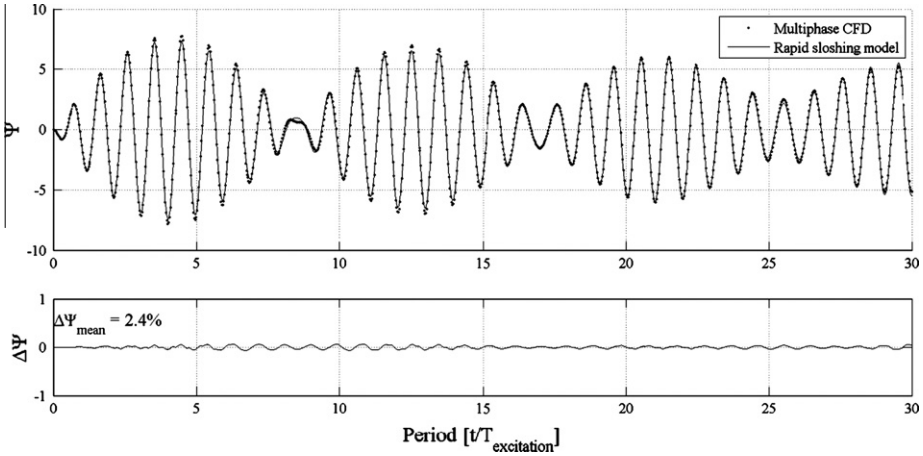

Fig. 10. Comparison of normalised fluid momentum Ψ for surge with excitation period $T = 1.10T_1$.

where L is the length of the tank and $m = 1, 2, 3, \ldots$. Usually, the first resonant period T_1 is the most crucial. For more complicated tank shapes such as the transverse cross section, the boundary element-based potential flow code FSIAP [25] is used to determine the resonant period. Table 1 summarises the key properties of the two sections.

2.2. Test problems

The first set of tests consists of surge motion with a range of excitation periods from $0.80T_1$ to $1.10T_1$ and an excitation amplitude of 0.015 m. The case with excitation period $T = 1.25T_1$ was used with the procedure in Godderidge et al. [13] to set up the

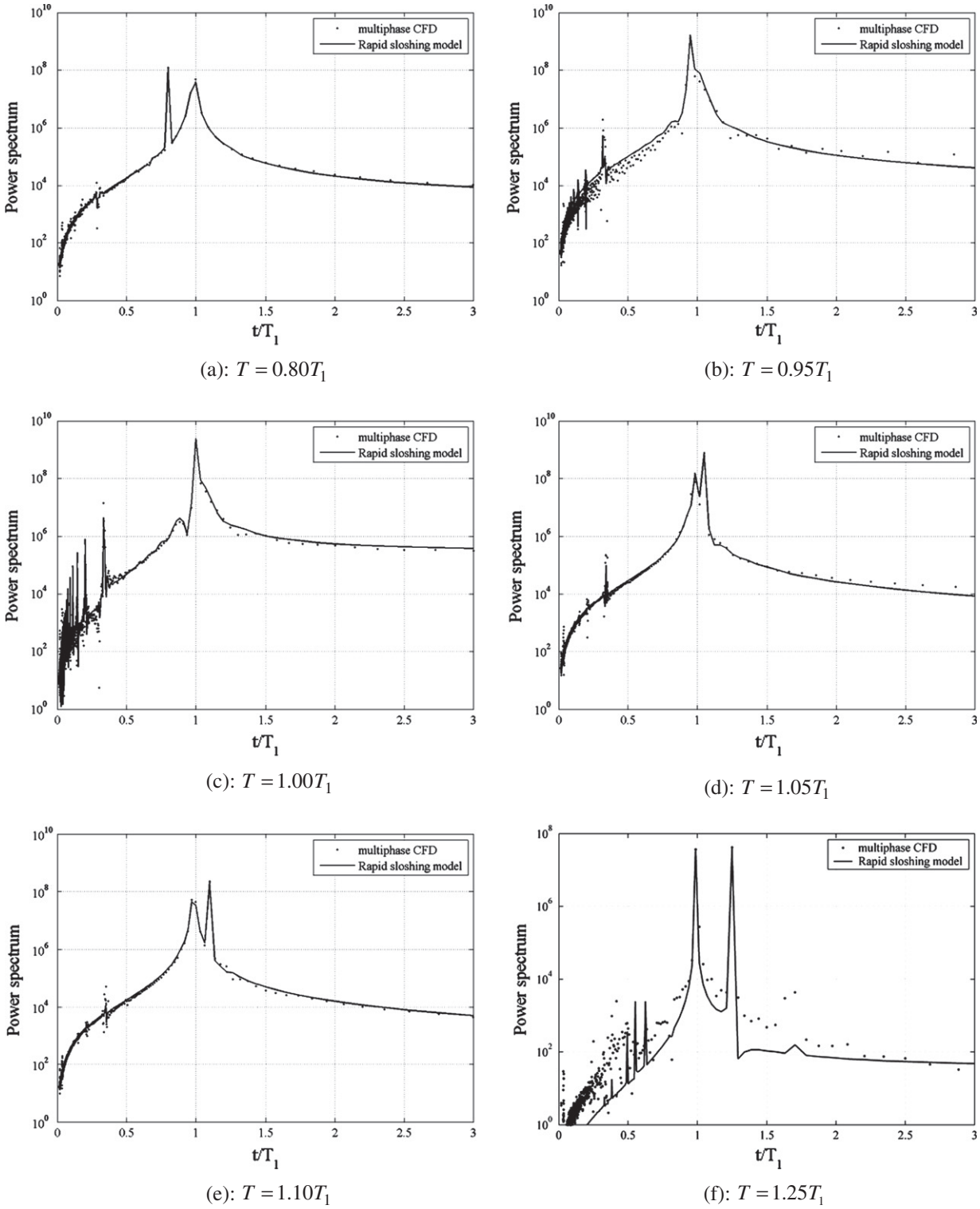

Fig. 11. Comparison of power spectra for surge induced sloshing.

sloshing model and it is not included as a validation problem. The pendulum sloshing model for the transverse cross-section is then set up with the same procedure using CFD data from sway induced sloshing with excitation period $T = 1.25T_1$ and displacement amplitude 0.025 m. Sway and roll validation problems consist of three excitation periods near the first resonant period. The sway and roll amplitudes are 0.025 m and 2°, respectively.

In stage three of the sloshing case study a irregular surge motion is applied to the longitudinal cross section and the effect of impacts is examined by increasing the tank height. The motion profile is obtained using a standard ITTC two-parameter wave spectrum [8], which can be written as

$$\frac{S(\omega)}{H_{1/3}^2 T_I} = \frac{0.11}{2\pi}\left(\frac{\omega T_I}{2\omega}\right)^{-5} \exp\left(-0.44\left(\frac{\omega T_I}{2\omega}\right)^{-4}\right), \tag{7}$$

where the significant wave height $H_{1/3}$ is 6 m, the wave period T_I is 10 s and ω is wave frequency. The relationship between the jth frequency component and the corresponding wave elevation A_j is given as

$$A_j^2 = 2S(\omega_j)\Delta\omega, \tag{8}$$

where $\Delta\omega$ is the constant difference between successive frequencies [8]. The resulting wave elevation is then given as

$$\varsigma = \sum_{j=1}^{N} A_j \sin(\omega_j t - k_j x + \varepsilon_j), \tag{9}$$

where k_j is the jth wave number, x is a location along the direction of wave propagation and ε_j is a random phase angle with a uniform distribution between 0 and 2π. This wave spectrum is selected because it is a broad band spectrum compared to other sea spectra. The resulting vessel acceleration profile is determined using ship-specific Response Amplitude Operators and scaling laws [21] and the power spectrum of the motion profile obtained is shown in Fig. 3. The second and third resonant sloshing periods, given by Eq. (5) as $T_2 = 0.62T_1$ and $T_3 = 0.50T_1$, are also in the range of excited motion frequencies. The simulation time is 200 s, which corresponds to approximately 35 min on a typical LNG carrier.

Stage four of the sloshing case study consists of five cases with coupled periodic surge and pitch motions with increasing levels of sloshing severity.

3. CFD model

CFD, the numerical solution of the Navier–Stokes equations, is established as a suitable methodology for the simulation of sloshing flows [22]. It is worth noting that accurate prediction of sloshing behaviour requires a systematic approach, validated against detailed experimental data recent workshops. Both interface tracking methods, such as Marker-and-Cell, and interface capturing methods such as the Volume of Fluid (VOF) method implemented using finite-volume discretisation are used in design and research. MAC is computationally efficient as it tracks the location of the free surface using massless particles and only the fluid is discretised [24]. However, flow phenomena such as fluid fragmentation and air entrapment cannot be simulated with MAC methods. The volume-of-fluid approach usually includes fluid and gas phases and can deal with violent sloshing beyond the limitations of theoretical models. Some recent examples of finite volume CFD sloshing simulation include Hadzic et al. [15] and Aliabadi et al. [2] and Godderidge et al. [11,12] compared the influence of homogeneous and inhomogeneous multiphase models for VOF simulation of sloshing. The application of VOF methods is restricted by its considerable computational costs and Dias et al. [6] have developed a numerical model which treats the discontinuities in the free surface and the mixing of gas and fluid using averaged quantities which is less computationally expensive.

3.1. Governing equations

An inhomogeneous multiphase model, which includes separate transport equations for mass, momentum and energy for every fluid provides a more faithful representation of the dynamic interaction between the fluids [19]. Godderidge et al. [11] validated the inhomogeneous multiphase model for a surge-induced sloshing flow with experimental results and Godderidge et al. [12] carried out further validation for sloshing impacts. In the inhomogeneous multiphase model, a full set of conservation equations is solved for each phase:

$$\frac{\partial}{\partial t}(r\rho) + \frac{\partial}{\partial x_i}(r\rho u_i) = m + \Gamma, \tag{10}$$

and

$$\frac{\partial}{\partial t}(r\rho u_i) + \frac{\partial}{\partial x_j}(r\rho u_i u_j) = -r\frac{\partial p}{\partial x_i} + \frac{\partial \tau_{ij}}{\partial x_j} + M^{\Gamma} + M^{r} + b_i, \tag{11}$$

and the stress tensor τ_{ij} is written as

$$\tau_{ij} = \mu\left(\frac{\partial u_i}{\partial x_j} + \frac{\partial u_j}{\partial x_i}\right), \tag{12}$$

where b_i is external body force (e.g. gravity), Γ mass transfer, μ dynamic viscosity, M^{Γ} momentum transfer due to mass transfer, M^r forces on the interface caused by the presence of the other phase, ρ density, p pressure, r volume fraction, u_i and x_i the Cartesian velocity and co-ordinate tensors. The mass and momentum transfer terms link the phase velocity fields. In the present problem there is no interphase mass transfer and the only remaining term is M^r.

This is computed using the relative velocity between the liquid and gas phases.

In the more widely used homogeneous multiphase model, this term is assumed to be large and hence there is no relative velocity between the phases [5]. Consequently, only one set of momentum conservation equations has to be solved. This reduces the computational effort by typically 60% [11]. However, Godderidge et al. [11] found that when simulating a nonlinear sloshing flow using CFD, the more complex inhomogeneous multiphase model should be used.

3.2. Discretisation

The governing equations are discretised using a finite volume method. Zwart [26] describes the discretisation procedure and Godderidge et al. [11] give the governing equations in their discretised form. In the present study a fully coupled solver, where the discretised conservation of mass and momentum equations are

Table 5
Rapid Sloshing Model settings for transverse cross section.

Length	0.7487
Effective mass fraction	0.59
Linear damping coefficient	0.23
Third-order damping coefficient	0.79
Restoring force: function	$\sin(\alpha\theta)$
Restoring force: coefficients	$\alpha = 0.99$
Impact model:	16°
Impact model: force coefficients	$a = 0.025$ $b = 15$
Impact model: damping coefficients	$c = 0.00025$ $a = 24$

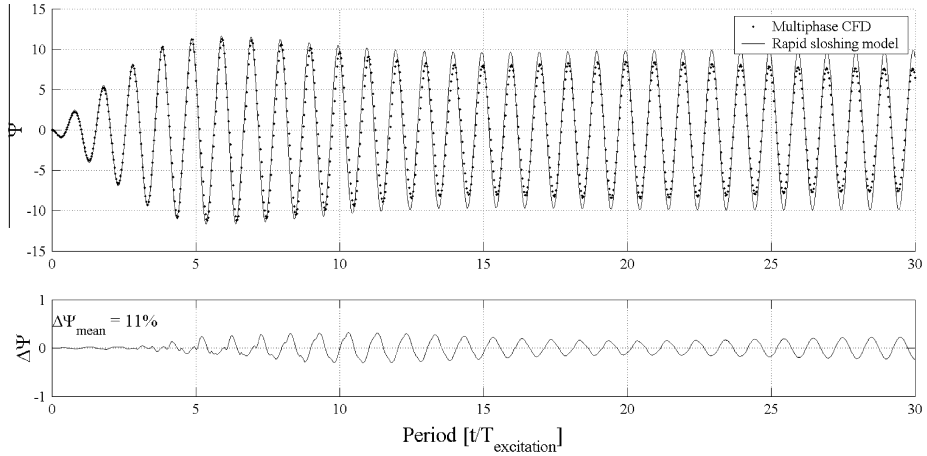

Fig. 12. Comparison of normalised fluid momentum Ψ for sway with excitation period $T = 0.95T_1$.

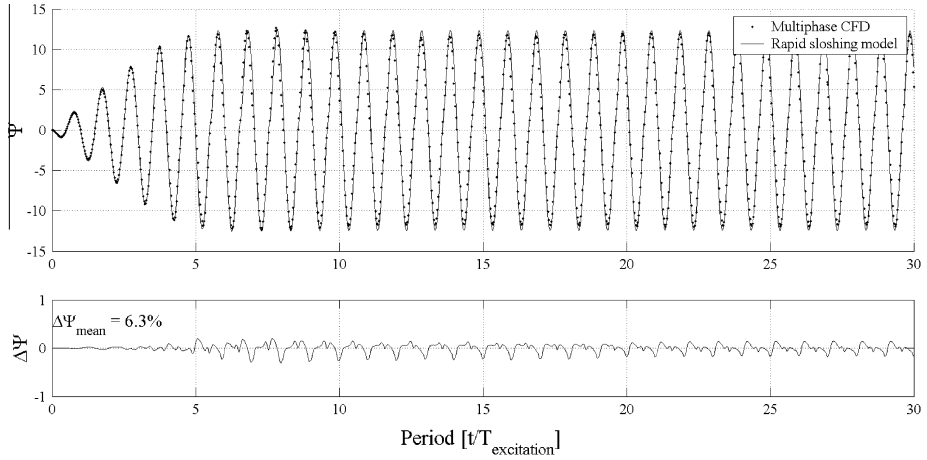

Fig. 13. Comparison of normalised fluid momentum Ψ for sway with excitation period $T = 1.00T_1$.

solved in a single system, is used. The problems with mass conservation reported by Godderidge et al. [11] are not encountered and mass is conserved to within 0.1% of the initial mass for simulations with more than 100,000 time steps. The advection scheme is based on the scheme by Barth and Jesperson [4] and the free surface is compressed by introducing an anti-diffusive flux in cells near the fluid interface [26,3].

The spatial discretisation scheme varies between a first and second order upwind scheme depending on the gradient [3]. It was found to be the most stable scheme. The sloshing motion of the container is applied using a body force approach. This approach adds additional time-dependent terms in the external body force vector b_i for translatory motions. When the tank is subjected to rotational motions, additional inertial forces are introduced which are accounted for with the introduction of corresponding terms in the conservation of momentum Eq. (11) [3].

The computational meshes for the longitudinal and transverse cross sections are shown in Figs. 4 and 5 respectively. The mesh densities and distributions are based on the mesh independence study for the longitudinal tank shape summarised in Table 2.

The longitudinal mesh contains 8745 elements (8109 hexahedral and 636 wedge) and the refined region at the top corners contains 5266 hexahedral elements. The transverse mesh contains 18,038 elements (16,767 hexahedral and 1326 wedge) and the refined region at the top corners contains 8016 hexahedral elements. The advantage of the hybrid grid approach used in this study is that only the regions of interest were refined while maintaining a hexahedral-dominant grid. This resulted in a more efficient use of computational resources.

3.3. Model parameters

The numerical investigations were carried out using the commercial CFD code CFX-11.1[1] and the computational parameters were selected based on the sensitivity study by Godderidge et al. [10]. It was found that the second order time marching scheme is most appropriate, as mass and momentum are conserved over a large number of time steps which is often requried for the simulation of violent sloshing. The magnitude of each time step was controlled dynamically using the root mean square of the local cell Courant number C_N computed over the entire velocity field. A maximum threshold value of $C_{N,RMS} = 0.15$ was identified in the validation study by Godderidge et al. [10] and the convergence criteria was applied in line with the recommendations given by ANSYS [3]. The computational parameters used in the simulations are summarised in Table 3.

[1] The simulations were run on a 64 bit, 2.2 GHz processor with 2 GB of RAM at the University of Southampton Iridis 2 computational facility.

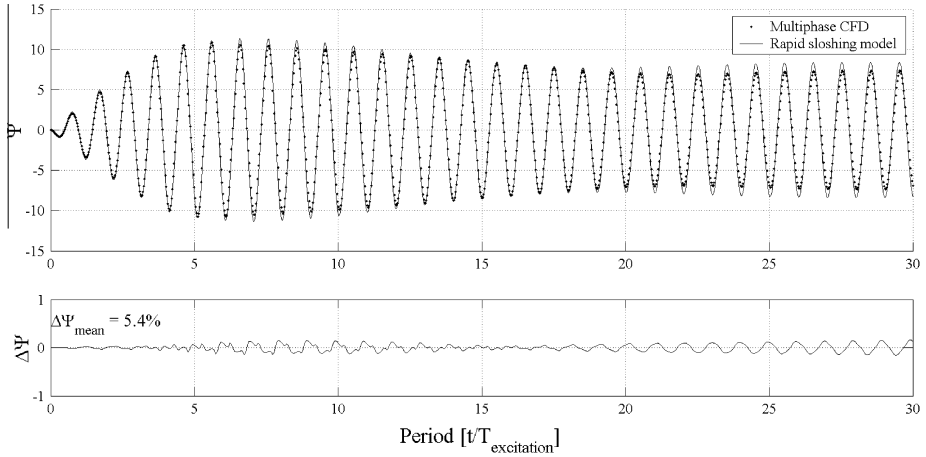

Fig. 14. Comparison of normalised fluid momentum Ψ for sway with excitation period $T = 1.05T_1$.

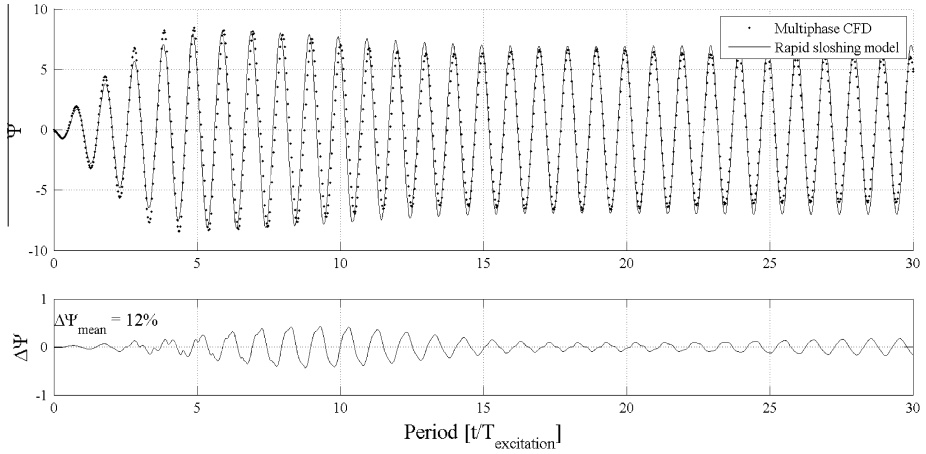

Fig. 15. Comparison of normalised fluid momentum Ψ for roll with excitation period $T = 0.95T_1$.

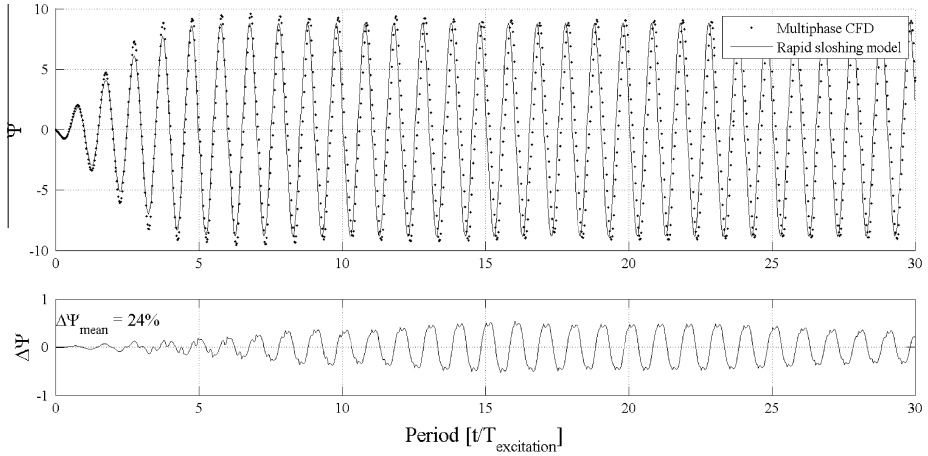

Fig. 16. Comparison of normalised fluid momentum Ψ for roll with excitation period $T = 1.00T_1$.

4. Results

The sloshing model given by Eq. (1) is validated by comparing its results for the sloshing flows identified in Section 3 with CFD results. These are independent of the corresponding solutions from the pendulum solutions model. The comparisons between the sloshing model and CFD are quantified using the horizontal fluid momentum, given as

$$P_{CFD} = \sum_i m_i u_i, \tag{13}$$

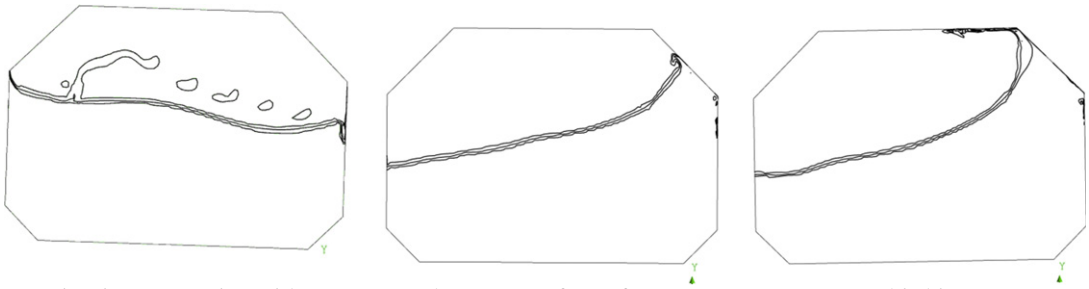

(a): First impact against side wall (b): Free surface after second impact (c): Third impact

Fig. 17. Volume fraction contours of V_{Water} = 0.05, 0.50 and 0.95 for transverse tank section subjected to roll motion with excitation period $T = 1.00T_1$.

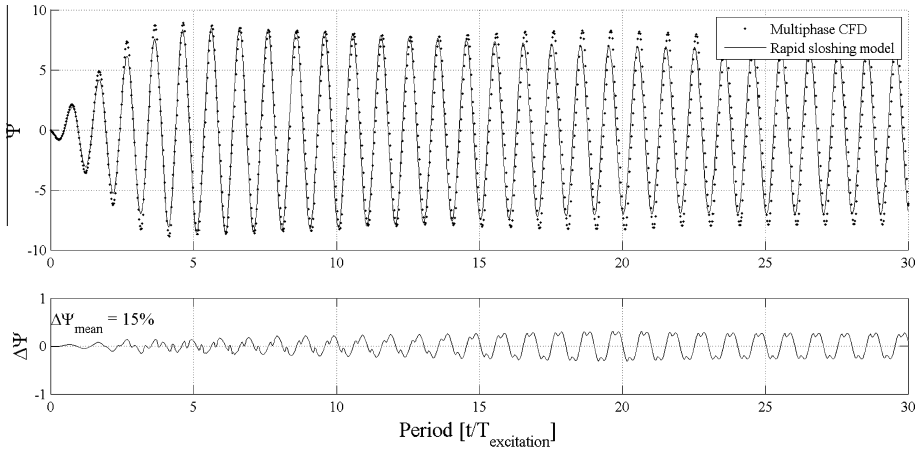

Fig. 18. Comparison of normalised fluid momentum Ψ for roll with excitation period $T = 1.05T_1$.

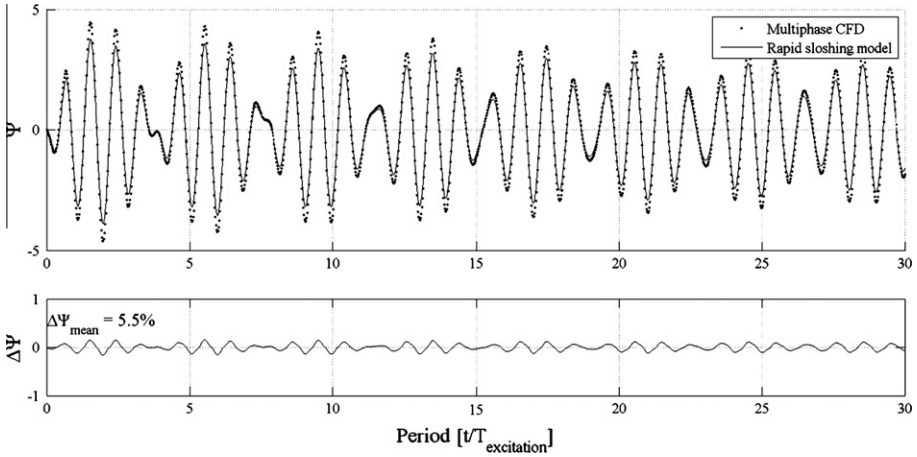

Fig. 19. Comparison of normalised fluid momentum Ψ for roll with excitation period $T = 1.25T_1$.

for the CFD result, where m_i is the fluid mass and u_i fluid velocity in the ith control volume. Horizontal fluid momentum is computed for the pendulum-based model as

$$P = l \cdot m_1 \cdot \dot{\theta} \cdot \cos(\theta), \tag{14}$$

where l is the pendulum length which is obtained using Eq. (14), m_1 the effective sloshing mass defined in Section 2.1 and θ the displacement angle. The calculated fluid momentum data are normalised as follows:

$$\Psi = \frac{P}{P_{rigid}}. \tag{15}$$

P_{rigid} is the momentum of the equivalent rigid body, given as

$$P_{rigid} = m_1 \dot{x}, \tag{16}$$

where $\dot{x}$ is the velocity imposed on the tank by Eq. (4). The difference between the two results is computed as

$$\Delta\Psi = \frac{P_{CFD} - P}{\max(P_{CFD})}, \tag{17}$$

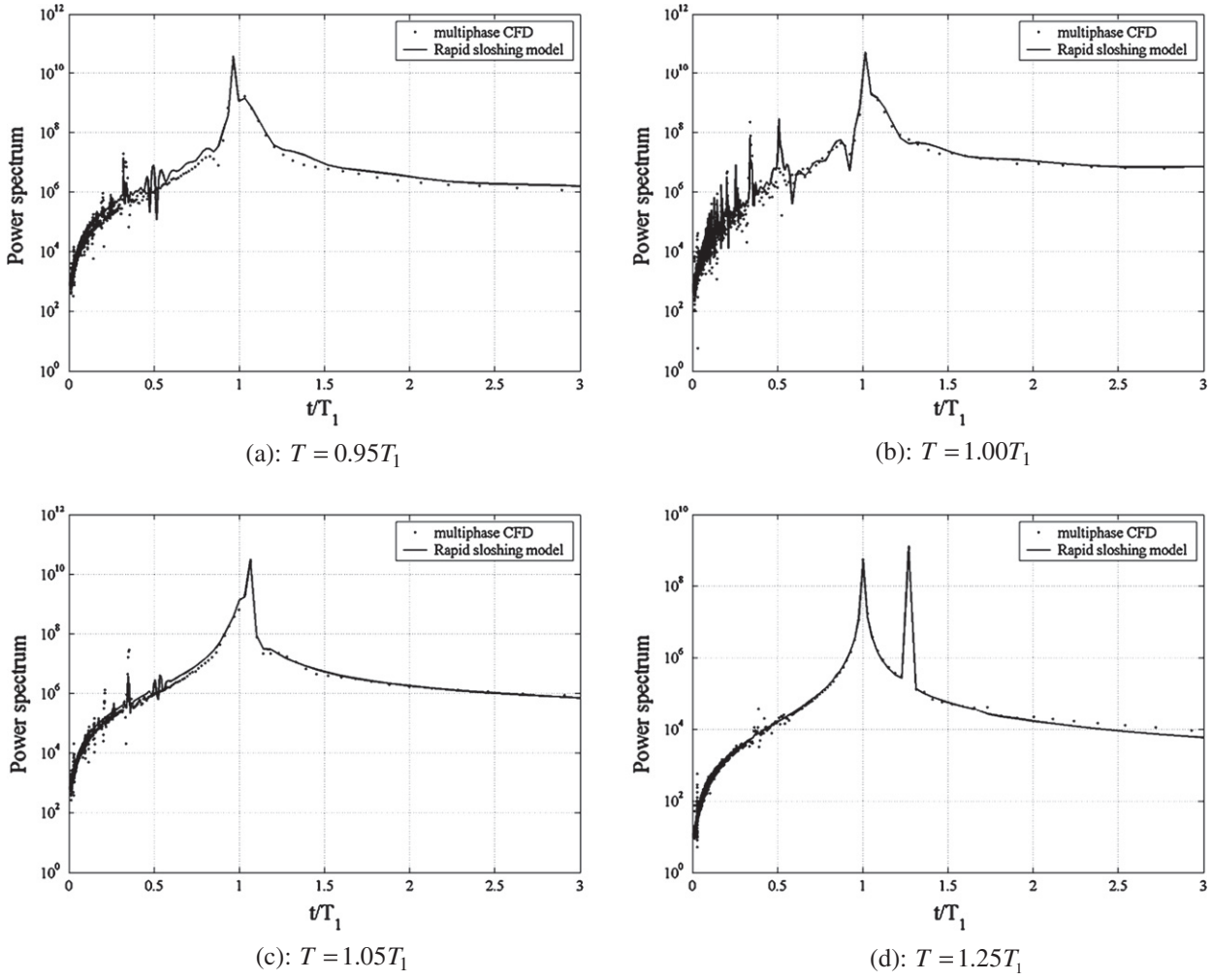

(a): $T = 0.95T_1$ (b): $T = 1.00T_1$

(c): $T = 1.05T_1$ (d): $T = 1.25T_1$

Fig. 20. Comparison of power spectra for sway induced sloshing.

and the mean rectified difference for n time steps is defined as

$$\Delta\Psi_{mean} = \frac{1}{n}\sum_{i=1}^{n}\frac{|P_{CFD} - P|_i}{\max(P_{CFD})}. \quad (18)$$

4.1. Longitudinal tank section

4.1.1. Surge

The longitudinal cross section is subjected to translatory motions in the first part of the sloshing case study. The excitation amplitude is 0.015 m for all surge cases and the excitation periods are $T = [0.80, 0.95, 1.00, 1.05, 1.10]T_1$. Table 4 summarises the settings for the Rapid Sloshing Model for the longitudinal cross section. The restoring force uses a third-order polynomial which was obtained by curve fit and this was carried out to confirm the applicability of the method to a restoring force which may not be adequately described with a periodic function such as sin.

The result for the highest excitation frequency case with an excitation period $T = 0.80T_1$ is shown in Fig. 6. A linear sloshing response [18] is observed and there are no impacts at the tank top. There is a good match between the CFD result and the pendulum sloshing model, but there are some small differences during the troughs of the periodic beating. The mean error is 2.6% and the error peaks are between the beating phases.

The second surge validation case, shown in Fig. 7 uses an excitation period $T = 0.95T_1$. The sloshing response is weakly non-linear and there are impacts occurring between oscillations four and eight. The predictions match the CFD results with reasonable accuracy, but the mean error is 11%. The attenuation in the CFD result is caused by the fluid near the tank top wall interacting with the air and this is not included in the sloshing model. The mean error value is somewhat pessimistic as the Rapid Sloshing Model solution is slightly out of phase with the CFD solution.

The excitation period and sloshing resonance are coincident in the next validation case. The momentum histories are compared in Fig. 8 and there is again good agreement between both results. The impacts against the tank ceiling continue throughout the duration of the simulation and the flow physics observed in the sloshing flow are captured by the impact model. The error stabilizes after about seven oscillations and the error envelope remains constant for the remainder of the simulation. The mean error of 5.8% is mostly due to the small phase difference between the two solutions.

The tank surge period is now increased to $T = 1.05T_1$ and the sloshing response is weakly nonlinear. There are no impacts at the tank ceiling but the CFD solution indicates that the interaction between the sloshing fluid and air near the tank ceiling affects the sloshing behaviour as in the case with $T = 0.95T_1$. Fig. 9 compares Ψ obtained from the CFD simulation with the pendulum results. The peaks in the second beating phase predicted by the sloshing model are about 15% greater than those obtained using CFD and the overall mean error is 13%.

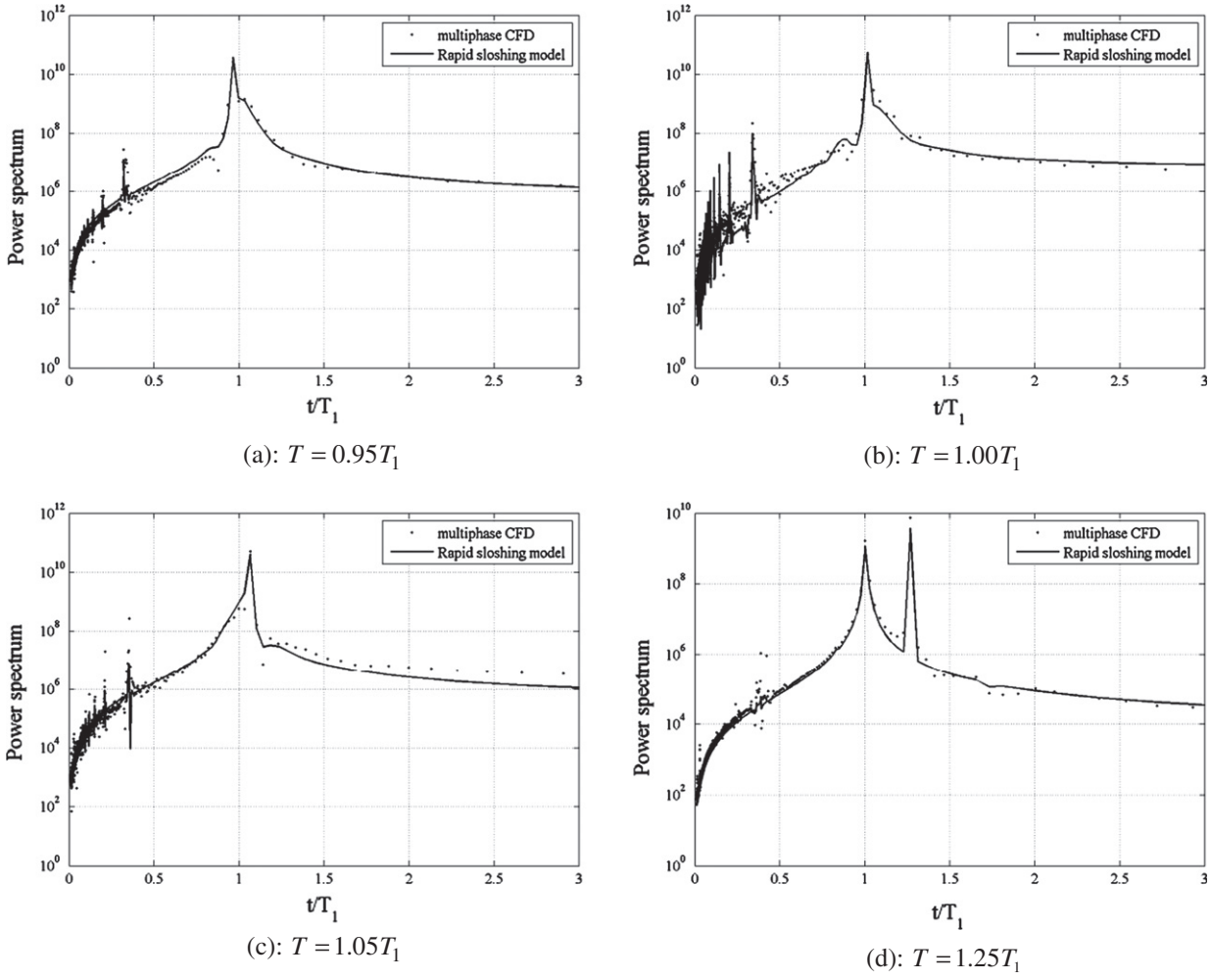

Fig. 21. Comparison of power spectra for roll induced sloshing.

The final validation case for surge increases the excitation period to $T = 1.10T_1$. The CFD and sloshing model momentum histories are compared in Fig. 10. The beating behaviour is well developed and is attenuated gradually. In this case, the CFD and sloshing model solutions show excellent agreement throughout the time frame considered and the mean difference of 2.4% is similar to that observed in Fig. 6.

4.1.2. Analysis

A frequency domain analysis is carried out for the sloshing flows modelled in Fig. 6–10 and the results are given in Fig. 11. When the excitation period is located sufficiently far from resonance as is the case in Fig. 11a, e and also f, two distinct peaks at the first resonance period and excitation period can be observed. In the surge simulation with $T = 0.95T_1$, shown in Fig. 11b, there is no separate peak at the excitation frequency and the spectrum is similar to that for the resonance case where the response peak coincident with the excitation period. In both cases, there is a distinct trough at the high-frequency side of the response peak and the low frequency side decreases gradually. For the sloshing flows with an excitation period of $T = 1.05T_1$ and $T = 1.10T_1$, shown in Fig. 11d and 11e respectively, there is a double peak at the resonance period and excitation period.

In all cases, there is good agreement in the low frequency range, which indicates the correct choice of damping coefficient and the high frequency behaviour up to approximately $0.5T_1$ is also well represented by the sloshing model. There are some differences in the case $T = 1.25T_1$ which was used to set up the model in Fig. 11f. The magnitude of the response is several orders of magnitude less than in the other cases and the time history, shown in Part 1 [13], shows excellent agreement with the CFD solution.

4.2. Transverse tank section

The second stage of the sloshing case study uses the transverse tank cross section in Fig. 2. The excitation periods $T = [0.95, 1.00, 1.05, 1.25]T$ are located near the first resonant period to capture the most significant sloshing responses. The sloshing model is adapted to this tank geometry by applying the procedure in Part 1 [13] to the CFD results obtained for sway with an excitation period $T = 1.25T_1$. Both sway and roll motions are validated and the tank displacement amplitudes are 0.025 m and 2°, respectively. Table 5 summarises the settings for the Rapid Sloshing Model for the transverse cross section. The same impact model coefficients as in the previous sections are used even though the impact physics are expected to differ between a rectangular and octagonal section.

4.2.1. Sway

The results for sway are considered first and the result for $T = 0.95T_1$ is shown in Fig. 12. It is interesting to note that the magnitude of Ψ is similar to that in the corresponding Fig. 7 for surge.

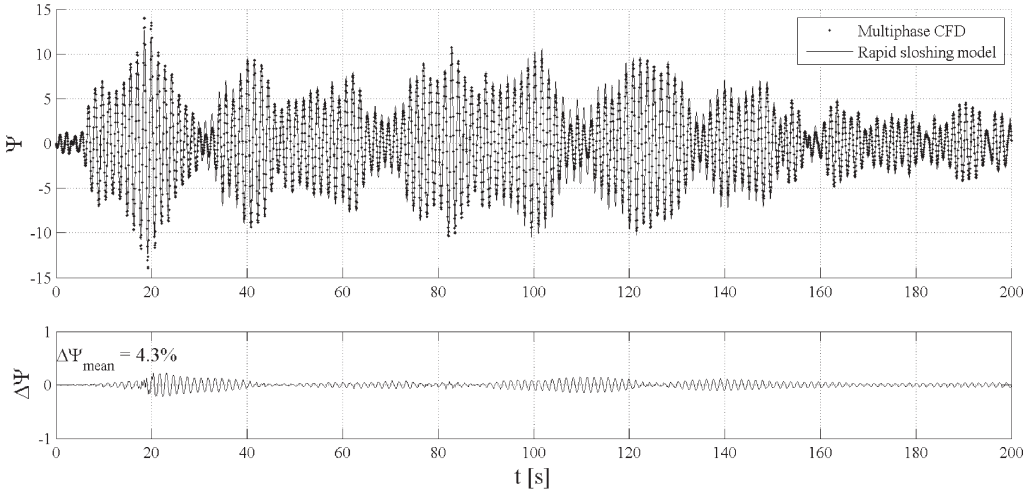

(a): full simulation

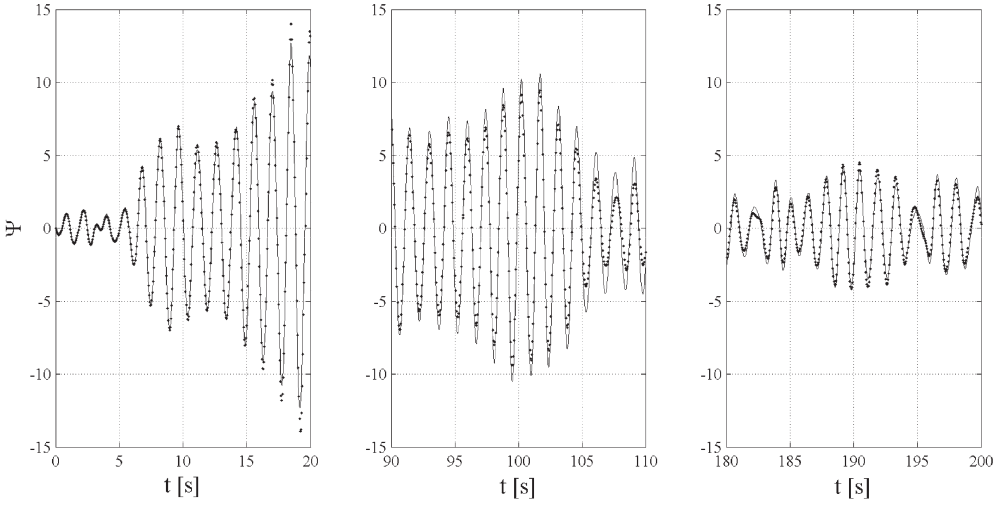

(b): zoom on regions of interest

Fig. 22. Comparison of normalised fluid momentum Ψ for irregular surge (case A).

During the initial transient there are impacts at the upper hopper and, to a lesser extent, the top wall, but these cease after about 15 oscillations. The sloshing model overestimates the steady-state CFD result for Ψ, but the transient is well predicted and the mean error of 11% is comparable to the corresponding case for surge. The error envelope remains constant after the initial transient phase and the difference in the results obtained can be attributed to the impact model.

The tank is excited at resonance in the second sway validation case, which is shown in Fig. 13. Impacts occur throughout this simulation and the sloshing model replicates this behaviour with good accuracy. The difference between the two results is constant after about 10 oscillations and the mean error is 6.3%.

The final sway test case is with an excitation period $T = 1.05T_1$ and the resulting fluid momentum plot is shown in Fig. 14. The initial transient region is well captured with the Rapid Sloshing Model and although there are discernable differences as the flow approaches a steady state, the mean error for the time frame investigated is 5.4%. Thus, the procedure in procedure for adapting the pendulum model to a specific tank shape given in Part 1 [13] is suitable for the tank shapes likely to be encountered during LNG sloshing analysis.

4.2.2. Roll

The next set of validation cases is roll-induce sloshing. The roll centre of motion is defined at the centre of area of the cross section which requires the use of the two-degree of freedom model in Eq. (1) to move the roll centre to the initial fluid centre of mass. The contribution of the sway component caused by shifting the centre of rotation to the quiescent fluid centre of mass is not found to be particularly significant but when it is neglected a different motion history is obtained for low frequency excitations. All model parameters are kept the same as in the sway – induced sloshing simulations in the previous section.

The first test uses an excitation period $T = 0.95T_1$ and the fluid momentum is shown in Fig. 15. There are some discernable differences between the CFD solution and sloshing model in the initial transient region where the CFD solution is leading the sloshing model. This does not continue into the steady state region and the mean error of 12% is comparable to values observed with transversely excited sloshing simulations discussed previously.

The second test, shown in Fig. 16, excites the sloshing tank at resonance and fluid impacts occur throughout the simulation. Fig. 17 shows three snapshots of the CFD solution, where Fig. 17a depicts the first impact against the vertical side wall. There are still

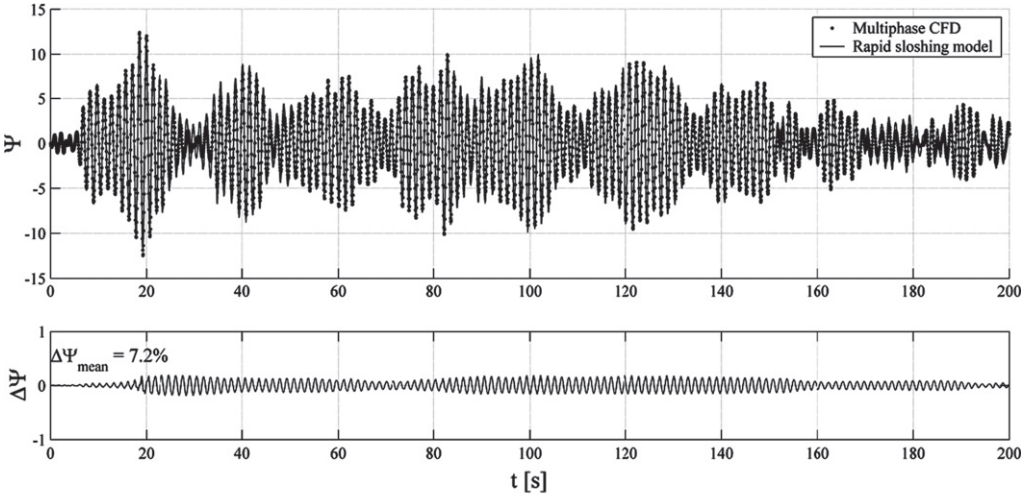

(a): full simulation

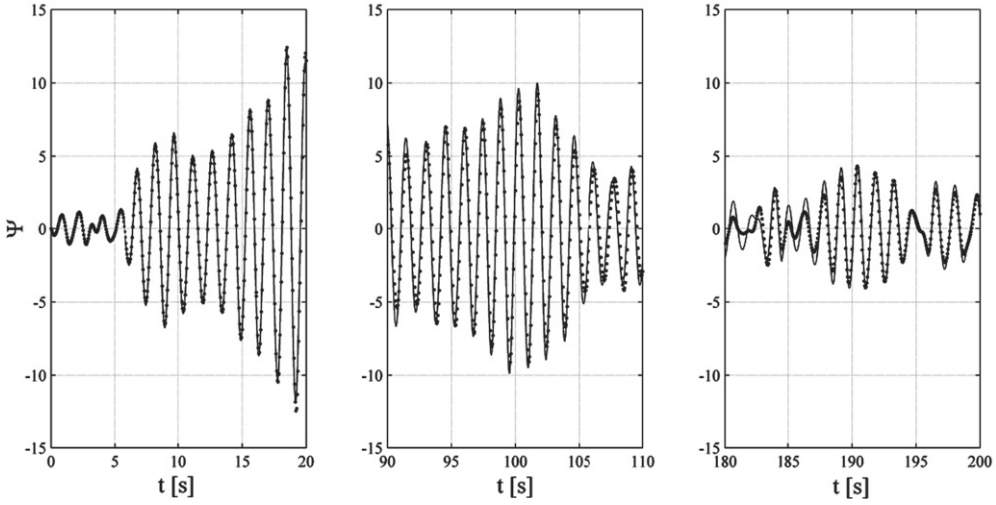

(b): zoom on regions of interest

Fig. 23. Comparison of normalised fluid momentum Ψ for irregular surge with raised tank ceiling (case B).

small quantities of fluid from the previous impact coalescing with the main bulk of fluid. In Fig. 17b the flow has progressed past the second impact at the upper hopper and is moving towards the third impact at the corner between the upper hopper and the tank ceiling. The post-impact flow field is shown in Fig. 17c. It is reversing its direction and there is some fluid fragmentation at the tank top. The mean difference of 24% is a pessimistic prediction as the main source of error is the small phase difference between the Rapid Sloshing Model and CFD solutions.

The next example in Fig. 18 uses the larger excitation period $T = 1.05T_1$ and there is more significant disagreement between the CFD result and the sloshing model. While the two solutions remain in phase, the transition between the start-up transient and the steady state flow field is not as well predicted as in the previous cases. This may be attributable to the fluid impact, where the three separate phases of fluid impact are not adequately represented with a single potential function.

The excitation period is increased further to $T = 1.25T_1$ for the final roll test. In this case, the non-periodic behaviour seen previously with surge is observed in Fig. 19 as well. The momentum history obtained CFD shows generally good agreement with the sloshing model and the error remains constant during the duration of the simulations. There are some differences in the flow evolution between the beating peaks and the mean error is 5.5%.

4.2.3. Analysis

Figs. 20 and 21 show the frequency domain analysis for the sloshing cases in the transverse cross section. In the sway cases the dominant peak is located at the excitation period, with a secondary peak at resonance. This peak is well defined in Fig. 20d, but in Fig. 20a and c there is no separate peak at the resonant frequency. The Rapid Sloshing Model solution predicts the knuckle in Fig. 20a, but there are differences at resonance in Fig. 20c. The value and location of the peak in the spectrum is well predicted by the Rapid Sloshing Model solution in all four cases considered and the solutions from the CFD and the sloshing model show good agreement in the low frequency range.

The results for roll in Fig. 21 are similar, with a dominant peak at the excitation frequency and secondary peaks at resonance. There is good agreement between Rapid Sloshing Model and CFD in the spectrum in Fig. 21a with the peak at the excitation frequency and knuckle at resonance well predicted by the Rapid Sloshing Model. A similar result is observed in Fig. 21b where the peak is at resonance. A secondary peak at $T = 0.4T_1$ is also

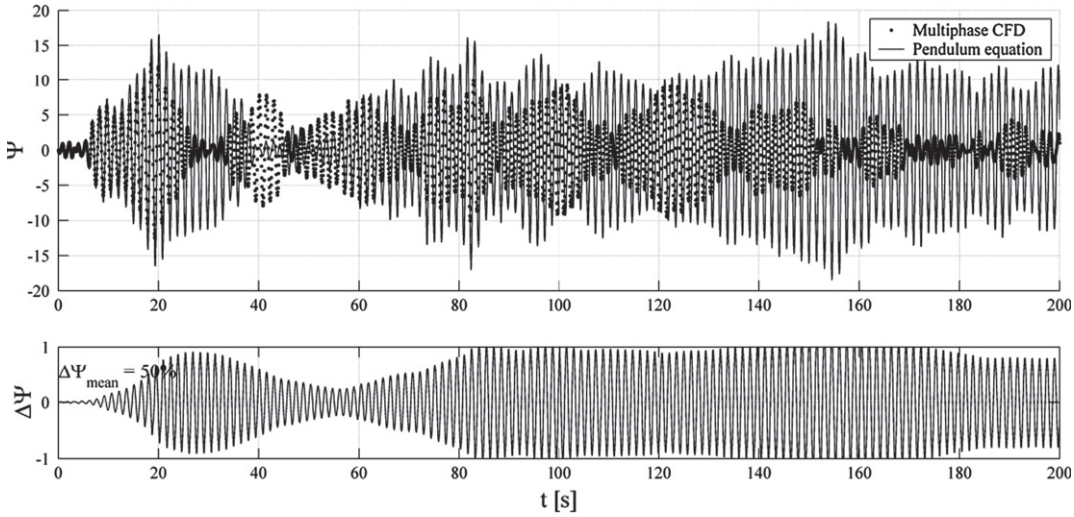

(a): pendulum equation with sin (θ)

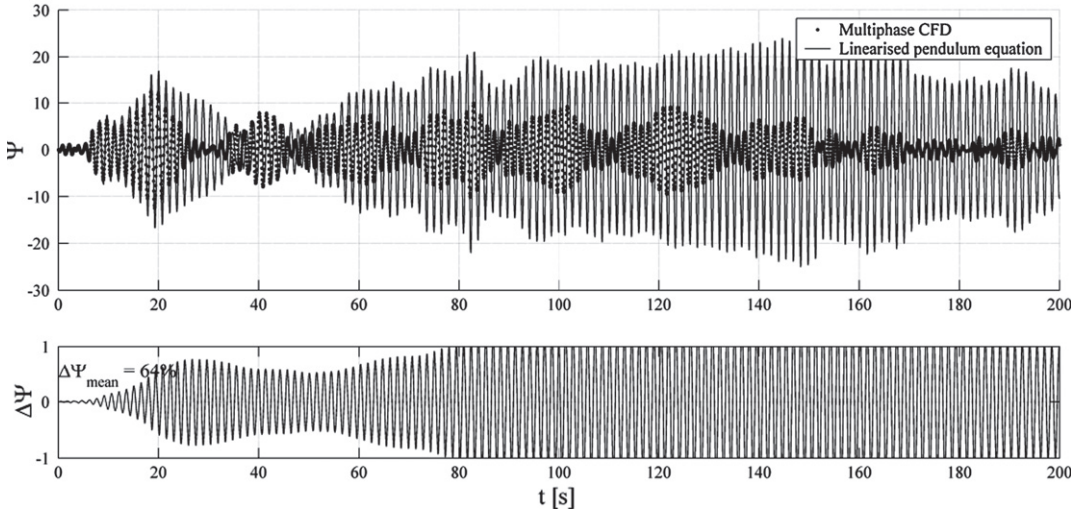

(b): linearised pendulum equation

Fig. 24. Comparison of normalised fluid momentum Ψ for case B with conventional pendulum models.

reasonably well predicted with the Rapid Sloshing Model solution and the low frequency behaviour of the Rapid Sloshing Model solution matches that of the CFD solution. Although the response peak is well predicted in all four roll validation cases, the Rapid Sloshing Model and CFD solutions in Fig. 21c show more substantial differences in the low frequency region. Better agreement and two distinct response peaks are observed in Fig. 21d and the low frequency behaviour of the Rapid Sloshing Model solution is in good agreement with CFD.

4.3. Irregular surge motion

The two previous validation stages for surge, sway and roll have all assumed that the excitation motion is periodic. This type of motion regime cannot be expected from a real ship and the third stage of the sloshing case study investigates the response of the proposed sloshing model to a irregular surge motion profile.[2]

[2] The cases considered in this section are identified by upper-case Latin characters.

The first test (case A) is the direct application of the motion profile obtained from Eq. (9) to the longitudinal tank cross-section using the pendulum sloshing model settings from the surge validation study in Section 4.1.1. This is illustrated in Fig. 22a, where there is good agreement between the CFD solution and the sloshing model. The mean error of 4.3% is similar to those observed with periodic surge motions. The areas with more significant differences around 20 s, between 90 and 110 s and the last 20 s of the simulation are enlarged in Fig. 22b. After the motion is initiated the CFD and sloshing model solutions are coincident until the onset of the first impacts at about 20 s. There are subsequent differences between the two solutions, but the sloshing model and CFD solution soon regain agreement. Near the mid-point of the simulation at 100 s the momentum predicted by the sloshing model is about 15% greater than the CFD solution. Nonetheless, towards the end of the simulation where there is a non-periodic sloshing response, the two solutions are again in good agreement.

The second case B investigates the effect of the top wall impact on the sloshing response by increasing the tank height to 1.2 m. The resulting momentum history is shown in Fig. 23a, with a similar level of agreement as in the previous case.

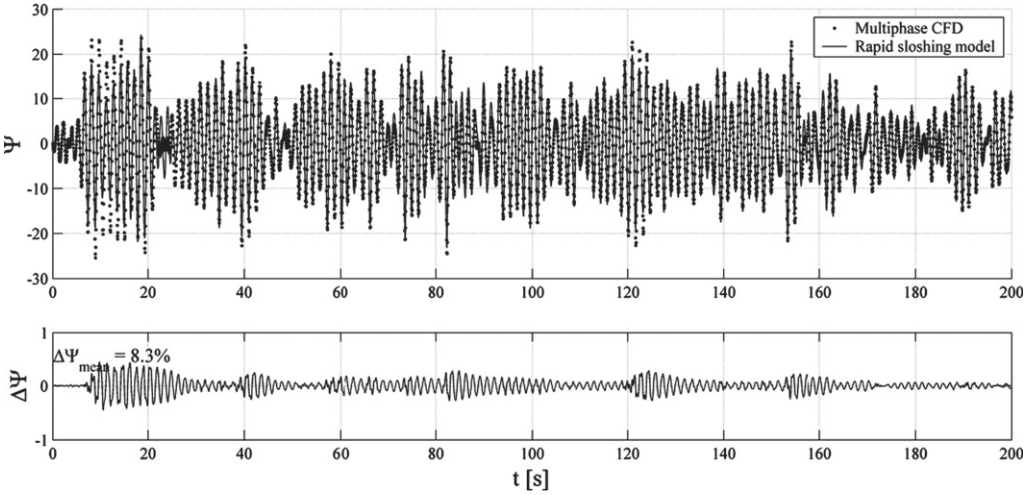

(a): full simulation

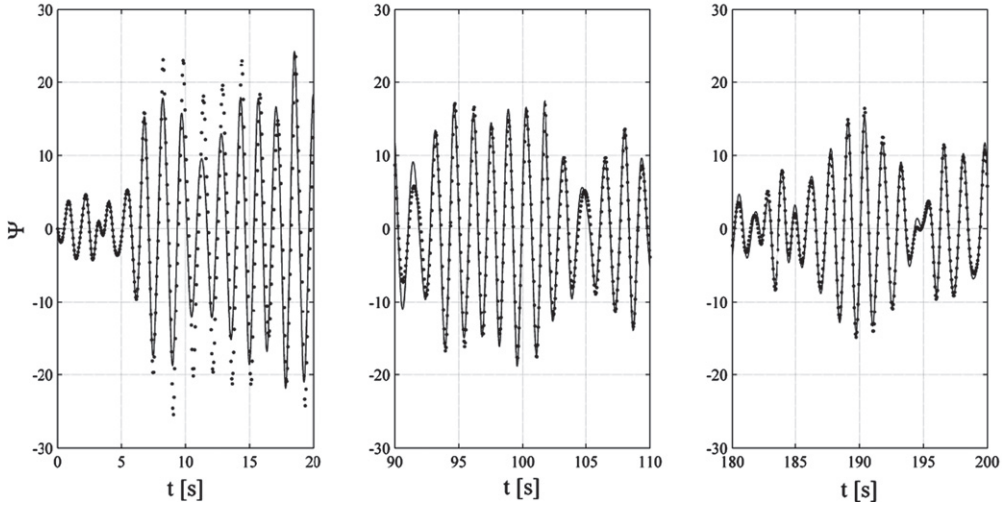

(b): zoom on regions of interest

Fig. 25. Comparison of normalised fluid momentum Ψ for irregular surge with raised tank ceiling and quadrupled acceleration amplitude (case C).

Although the mean error has increased to 7.2% in this case it is evenly distributed throughout the simulation. The three snapshots highlighted in the previous case are also examined in greater detail and the first momentum peak at 20 s is well predicted by the sloshing model. The CFD and sloshing model data for the subsequent flow evolution near 100 s show excellent agreement, but there are some more pronounced differences toward the end of the simulation at 180 s.

The motion profile in case B is also applied to a typical pendulum sloshing model with a $\sin(\theta)$ and a linearised restoring force term [7] and only a linear damping coefficient. Fig. 24 shows the effect of substituting the Rapid Sloshing Model approach adopted in this paper neither pendulum model can capture the sloshing behaviour after the first 10 s. The momentum predicted by the conventional pendulum models usually exceeds the CFD results but there is a phase between 35 and 45 where the pendulum models underestimate the momentum by about 75%. The linearised pendulum equation results in a slightly larger mean error of 64% compared to the 50% error with the normal pendulum equation.

The final validation case C with irregular tank motions introduces a more severe motion regime by using the same time series as in the previous two cases and increasing the acceleration magnitude fourfold. This produces greater nonlinearities in the sloshing response throughout the 200 s considered and the results, obtained using the 1.2 m high tank used previously, are shown in Fig. 25. The peak magnitude of Ψ has doubled and a comparison of the two plots in Figs. 23 and 25 illustrates some of the complexities of sloshing.

The maximum momentum occurs between 10 s and 20 s as in the previous case, but the transition is sharper and the Rapid Sloshing Model has some difficulties in replicating this behaviour. After about 25 s, there is again good agreement between the two methods and the next peak phase between 35 and 45 s is well predicted with the Rapid Sloshing Model. After about 80 s there is a significant peak in the momentum and the Rapid Sloshing Model and CFD solutions show good agreement in the snapshot between 90 and 110 s. There is a substantial spike at about 155 s, compared to the gradual decrease observed in Fig. 23 at the same time which underlines the nonlinearities in a sloshing flow and its sensitivity to history effects. In the final 20 s of that simulation, there is again agreement between the CFD solution and the Rapid Sloshing Model. The mean error of 8.3% is despite the substantial increase in motion amplitude very similar to that observed in other simulation.

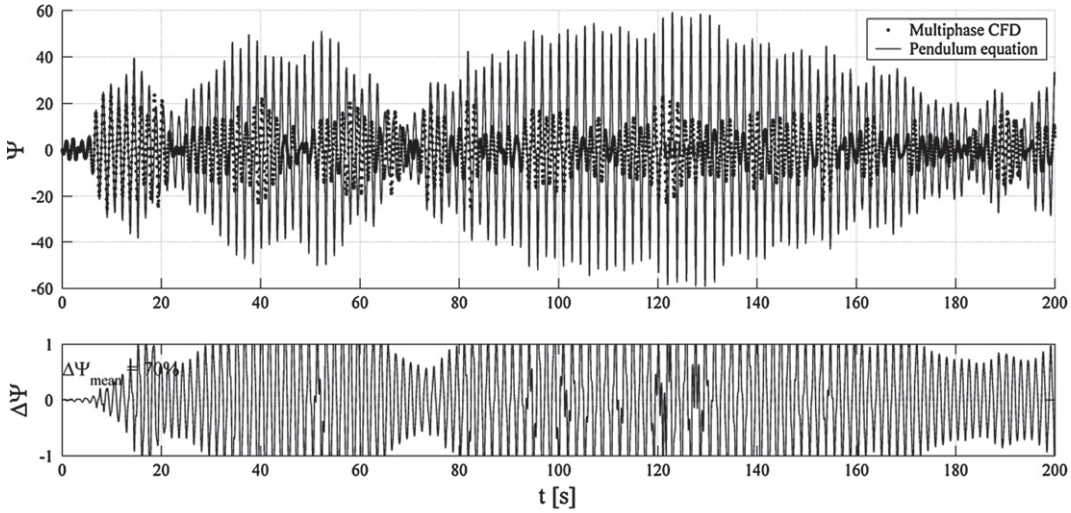

(a): pendulum equation with sin (θ)

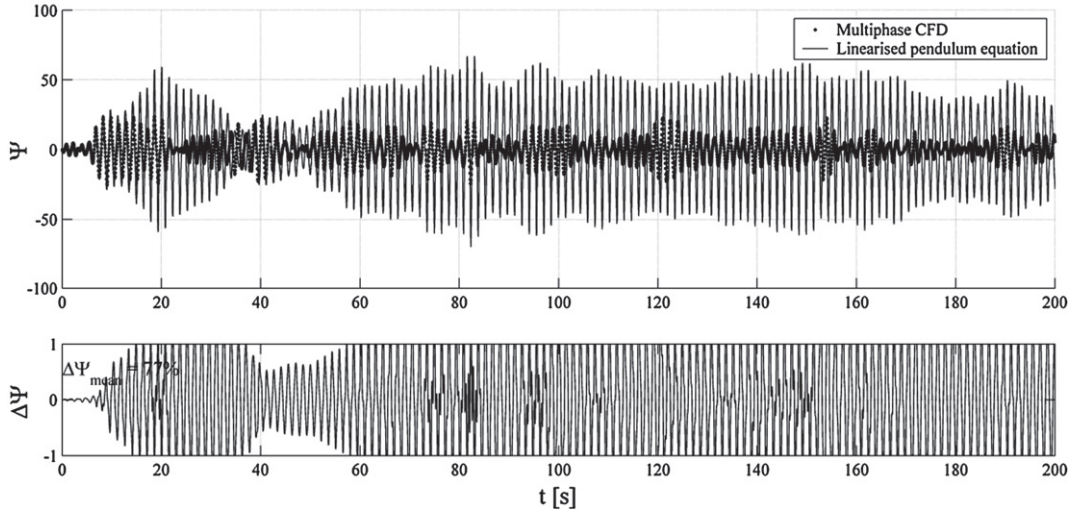

(b): linearised pendulum equation

Fig. 26. Comparison of normalised fluid momentum Ψ for case C with conventional pendulum models.

Case C is also simulated using the normal and linearised pendulum equations and the results are shown in Fig. 26. After about 10 s, both pendulum models fail to replicate the sloshing behaviour and the absence of an impact model results in further differences. The linearised pendulum equation generally over-predicts the fluid momentum and its mean error of 77% is only slightly larger than the 70% observed with a normal pendulum equation. This suggests that the key influence is the restoring force model rather than its linearisation.

The frequency domain analysis of the sloshing response obtained with irregular surge motion is shown in Fig. 27. The spectra for case A and case B are similar, with a well-defined peak at the first resonant frequency. When the excitation amplitude is increased, the response peak is broader but the shape of this spectrum is comparable to the other two. The solution was computed in fast time and most of the computational time was spent interpolating the motion profile on the time steps used for the numerical solution of the differential equations.

The momentum histories obtained with the RSM shown in Figs. 22–25 are used to obtain the dynamic sloshing force using the relation

$$F_D = \frac{\partial}{\partial t}(P), \tag{19}$$

where F_D is the dynamic force. The time derivative of momentum was calculated numerically using the GRADIENT function in MATLAB as a second order central difference scheme. The dynamic force is non-dimensionalised using the initial free surface height such that

$$\text{Non-dimensional force} = \frac{F_D}{\rho g h b}, \tag{20}$$

where b is tank width, g gravity, h filling height and ρ density. The corresponding values for F_D were obtained from the CFD simulation by integration of the dynamic pressure on the tank walls.

Fig. 28 compares the non-dimensional dynamic force for case A and there is agreement between the CFD and the RSM solutions. The mean error has increased from 4.3% to 7.5% which is mainly attributable to disagreements between 100 and 120 s as shown in Fig. 28b. The dynamic force in the initial transient phase with impacts is predicted with good accuracy using the RSM and Fig. 28a shows that the two solutions remain in phase throughout the 200 s time frame considered.

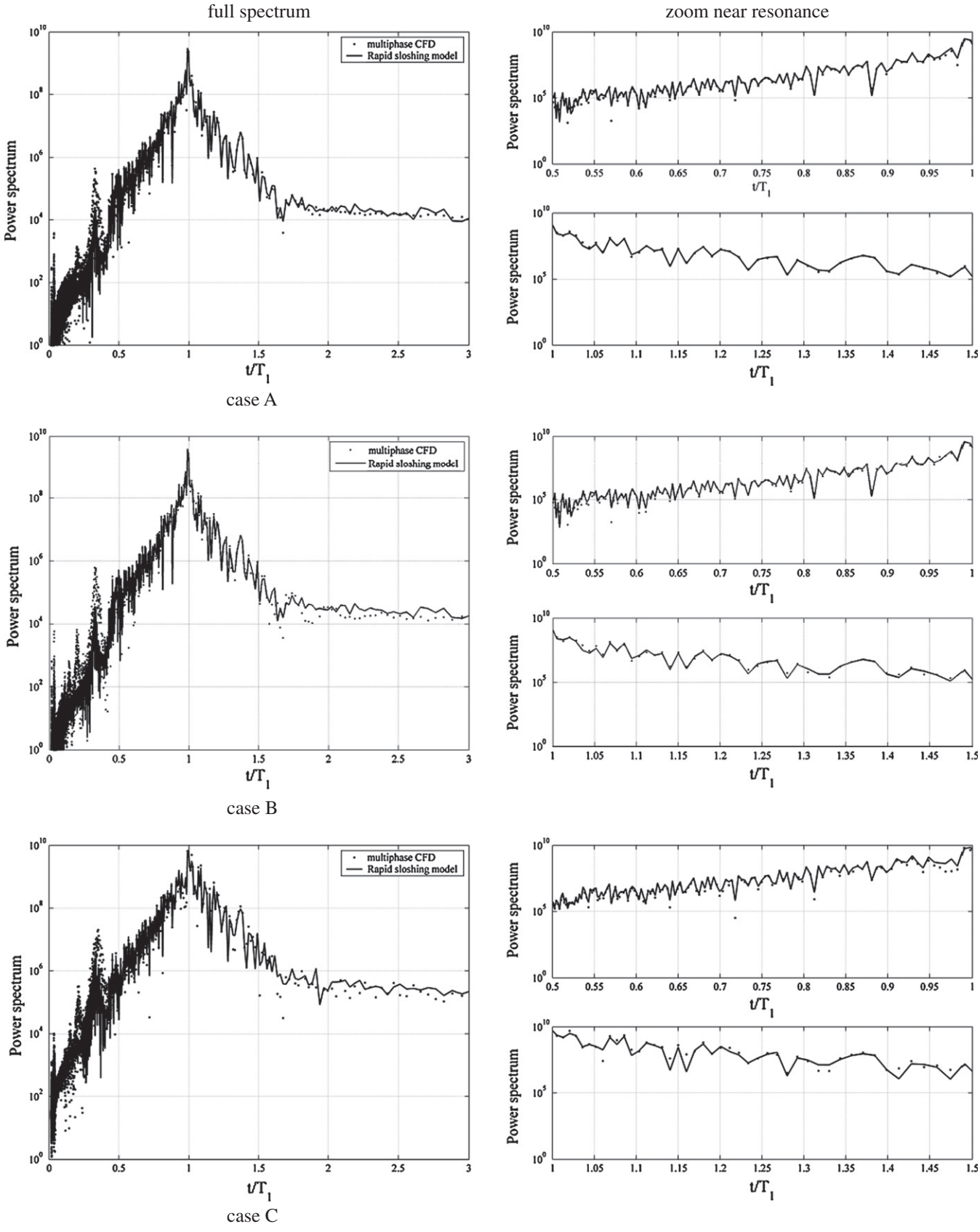

Fig. 27. Frequency domain analysis of the sloshing response for irregular surge (case A–C).

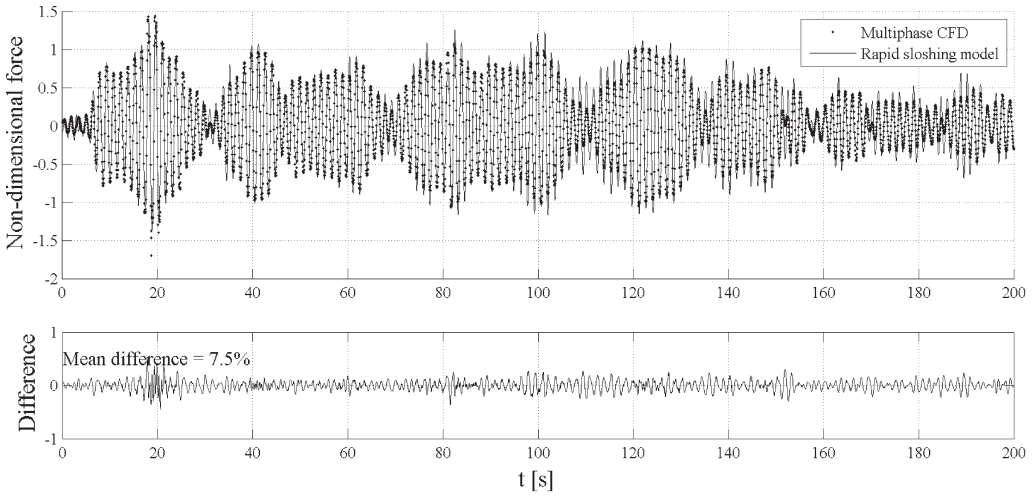

(a): full simulation

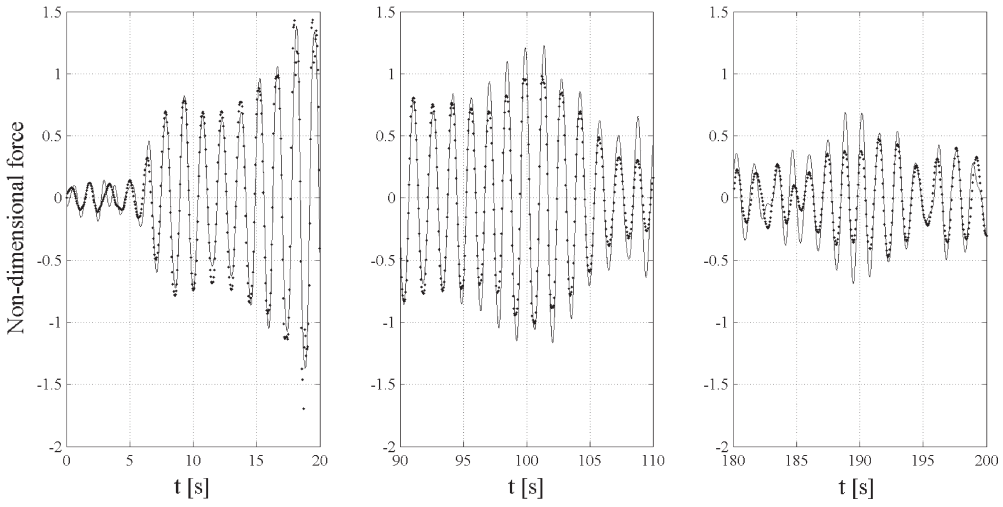

(b): zoom on regions of interest

Fig. 28. Comparison of RSM with CFD using normalised sloshing force on tank for irregular surge (case A).

The non-dimensional dynamic force for case B is shown in Fig. 29. The CFD and RSM solutions are in good agreement and the mean error of 8.3% for the momentum-based comparison in Fig. 23 is similar to the 9.6% observed using the dynamic force calculation. The peaks in the first 20 s of the simulation are reproduced with the RSM but the RSM overpredicts the force in the region between 100 and 120 s as shown in Fig. 29b.

The final comparison with the dynamic sloshing force is made using case C where the motion amplitude is increased fourfold and the comparison between the CFD and RSM solutions is shown in Fig. 30. In this case there are more significant differences between the CFD and RSM solutions in the initial 20 s and the mean error has increased to 13% compared to 8.3% in the momentum-based comparison. The force predictions from the RSM do not reproduce the peaks between 10 s and 20 s and the peaks at 122 s are missed. Otherwise the CFD and RSM solutions are in good agreement when using the dynamic force as a basis for comparison.

4.4. Combined surge and pitch

The final stage of the sloshing case study is the simulation of sloshing caused by the simultaneous surge and pitch motion of the tank.[3] The two-degree of freedom model in Eq. (1) was used in Section 4.2.2, but the sloshing response was dominated by the roll motion. In this section, five motion profiles with similar surge and pitch displacement amplitudes, chosen somewhat arbitrarily, are imposed on the tank. The centre of rotation is at the centre of area of the tank as in the corresponding experiment by Hinatsu [16]. The sloshing model settings are the same as in the surge validation study in Section 4.1.

In case a, shown in Fig. 31, the excitation motion is at resonance and the surge and pitch amplitudes are 0.015 m and 2°, respectively. There are fluid impacts after the first three oscillations and the impacts continue for the entire simulation. There is good agreement between the CFD solution and sloshing model throughout the duration of the simulation and the difference remains constant. The mean error of 7% is comparable to other cases considered in this sloshing case study.

The second validation case, case b, uses the same surge and pitch amplitude as in the previous case, but the excitation periods are different, with the surge excitation period at resonance and the pitch excitation period $T_{pitch} = 1.10T_1$. This case is unlikely to be experienced by a real ship as the motions are excited by the same wave profile, but this case illustrates the ability of the sloshing model to handle such motion profiles. The resulting sloshing response is depicted in Fig. 32 and, although there is some disagreement between the CFD solution between the beating

[3] The cases considered in this section are identified by lower-case Latin characters.

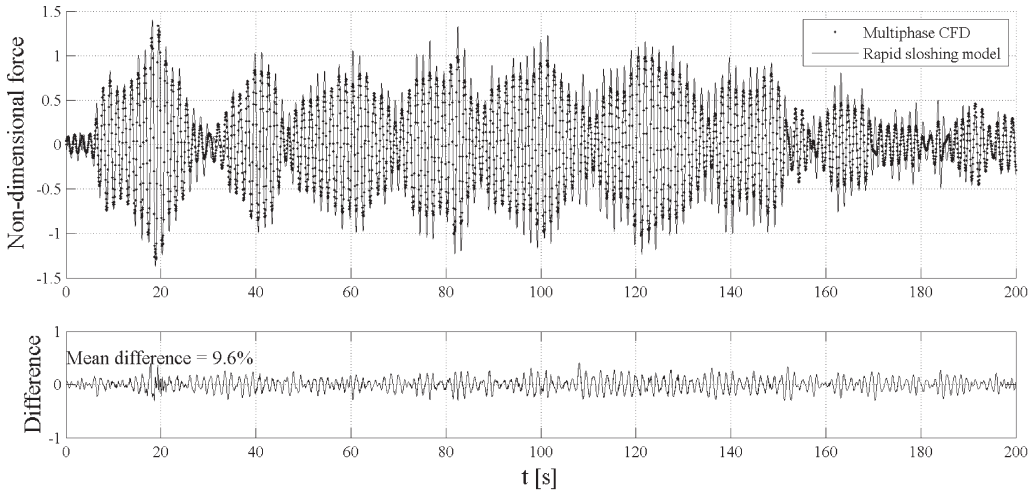

(a): full simulation

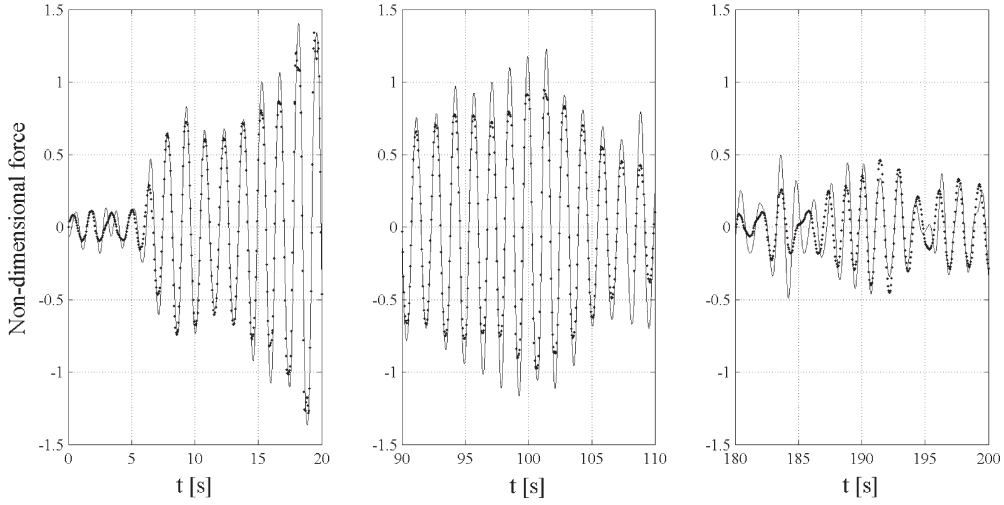

(b): zoom on regions of interest

Fig. 29. Comparison of RSM with CFD using normalised sloshing force on tank for irregular surge with raised tank ceiling (case B).

phases, the peaks during impact are predicted with good accuracy and the solutions are in phase throughout the 30 oscillations shown.

Case c, shown in Fig. 33, uses an excitation period $T = 1.0362T_1$ for both surge and pitch. The response is similar to that observed in Fig. 31 and the error envelope is similar with a mean error of 13%.

In the fourth two degree of freedom validation test case, case d, in Fig. 34, the pitch amplitude is increased to 5° and the surge period $T_{surge} = 0.95T_1$, which was more problematic for simulation using the proposed sloshing model. The fluid momentum peaks calculated using the pendulum model and CFD are of similar magnitude, but the two solutions differ when descending through $\Psi = 0$. This is explained by the impact model and the violent nature of the sloshing response. This is explained by the impact model and the violent nature of the sloshing response. The mean error of 16% is due to the difference between the solutions at at the initial transient which caused by the impact model.

Fig. 35 shows the free surface location during one half oscillation for case d. In Fig. 35a the flow has struck the top wall and a jet is forming which has progressed considerably in 0.15 s (shown in Fig. 35b). The flow direction is changing in Fig. 35c and the jet has reached the right side wall. A hydraulic jump forms close to the right wall in Fig. 35d and 0.05 s later the first fluid impact occurs at the right side wall as shown in Fig. 35e. During and after impact illustrate din Fig. 35f and g there is air entrapment and bubble formation and the fluid is moving up to the top wall. The impact against the top wall is shown in Fig. 35h and the post-impact jet is illustrated in Fig. 35i.

The frequency domain analysis of the cases considered in stage four of the validation is shown in Fig. 36. The spectrum for case a is similar to the pure surge resonance case, but the local trough on the high-frequency side of resonance is not replicated. The response spectrum for case b has two distinct excitation periods with a peak at the resonant frequency and a smaller separate peak at the pitch excitation period. There is a further peak near the resonance period and there is a distinct difference between the CFD solution and the sloshing model at the second resonant period $T_2 = 0.62T_1$.

The response spectrum of case c with identical surge and pitch excitation frequencies is similar to that in case a, although the peak is not as sharp. In both cases, the CFD and sloshing model spectra are similar at low frequency. The final case, case d, in Fig. 36 with

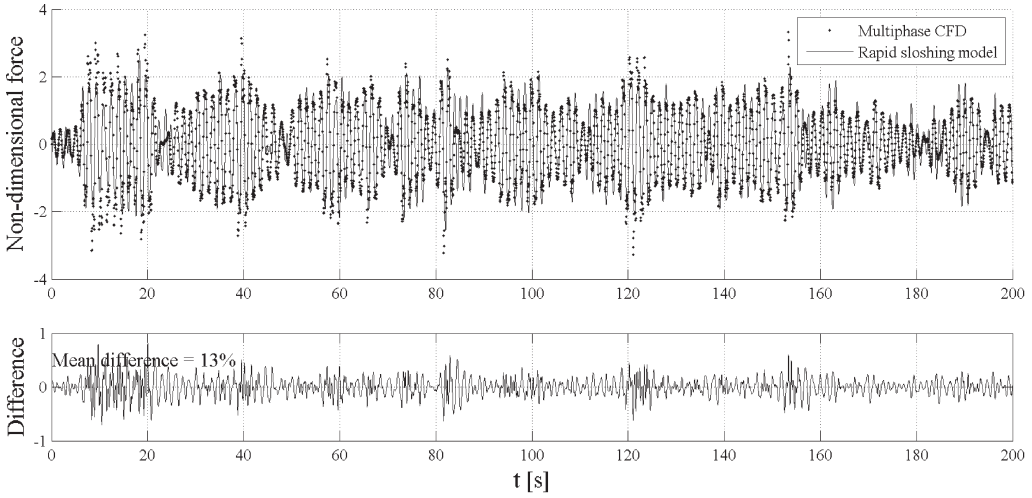

(a): full simulation

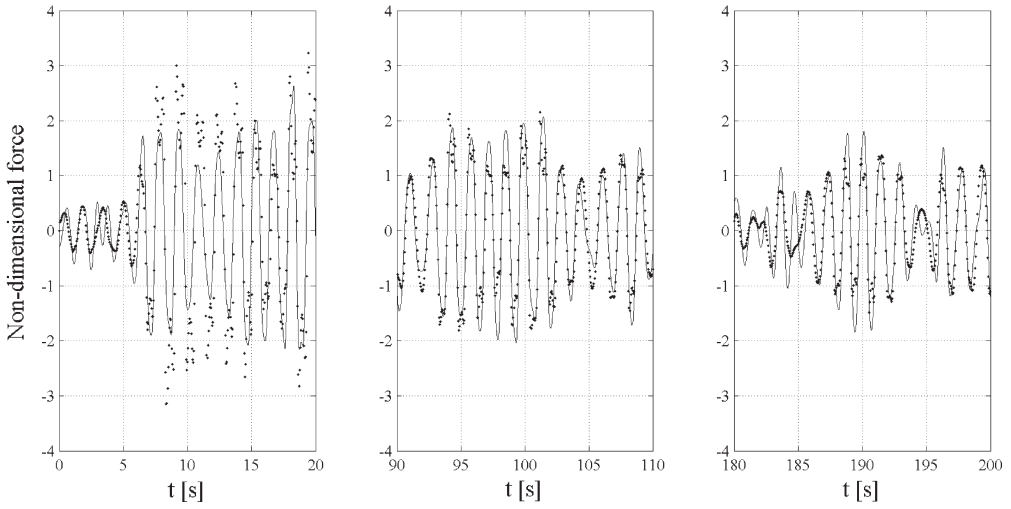

(b): zoom on regions of interest

Fig. 30. Comparison of RSM with CFD using normalised sloshing force on tank for irregular surge with raised tank ceiling (case C).

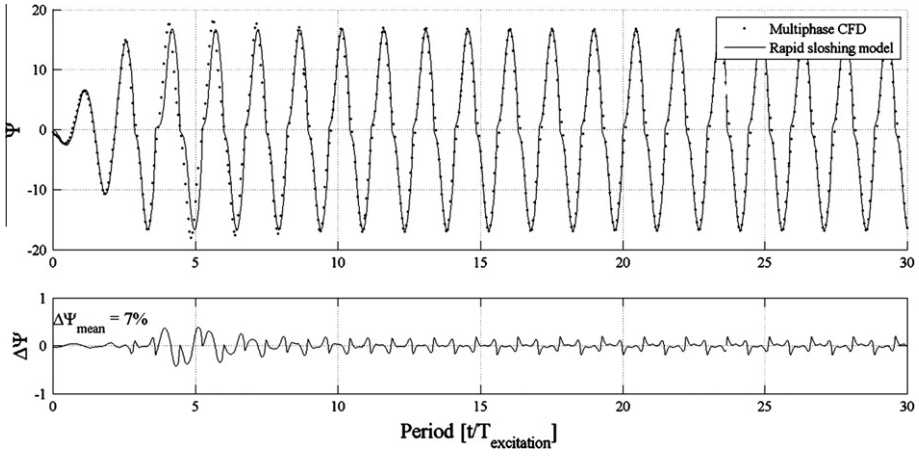

Fig. 31. Comparison of normalised fluid momentum Ψ for combined surge and pitch – case a.

increased pitch amplitude shows greater differences in the response spectrum. The distinct peaks near resonance are not captured well but the high frequency peak at $t/T_1 = 0.3$ is captured with surprising accuracy.

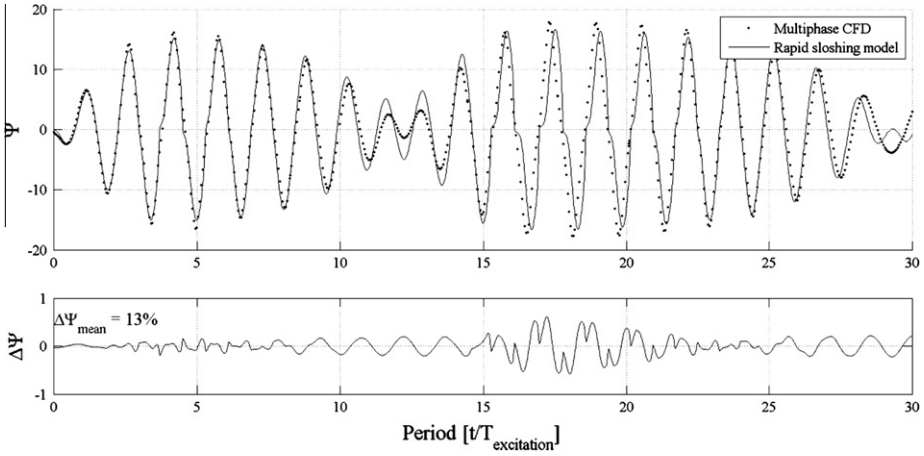

Fig. 32. Comparison of normalised fluid momentum Ψ for combined surge and pitch – case b.

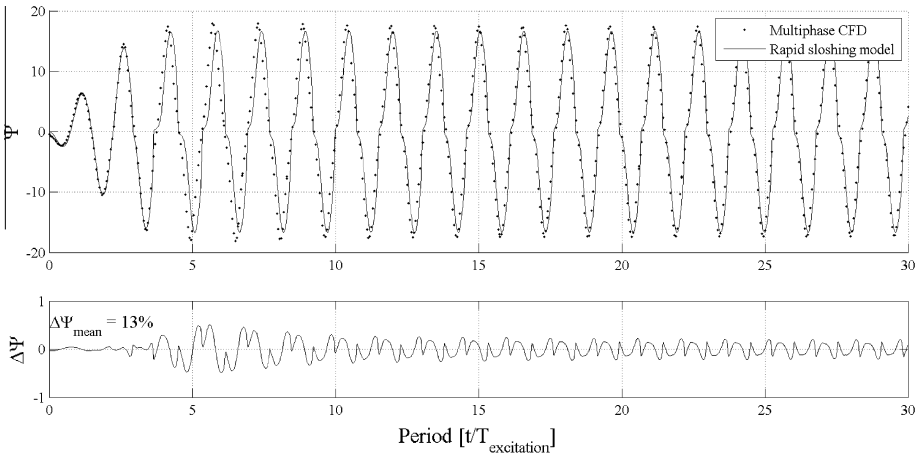

Fig. 33. Comparison of normalised fluid momentum Ψ for combined surge and pitch – case c.

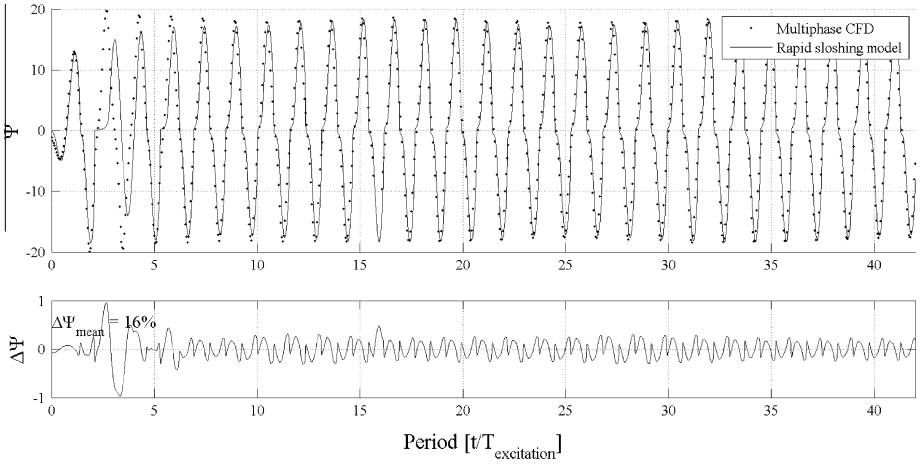

Fig. 34. Comparison of normalised fluid momentum Ψ for combined surge and pitch – case d.

Examples of the application of the Rapid Sloshing Model in simulations of coupled ship motion and sloshing can be found in Lee et al. [20]. A good overall agreement was found with other available numerical predictions and experimental measurements.

5. Conclusions

The sloshing model introduced in Part 1 [13] is applied to a sloshing case study for longitudinal and transverse cross sections

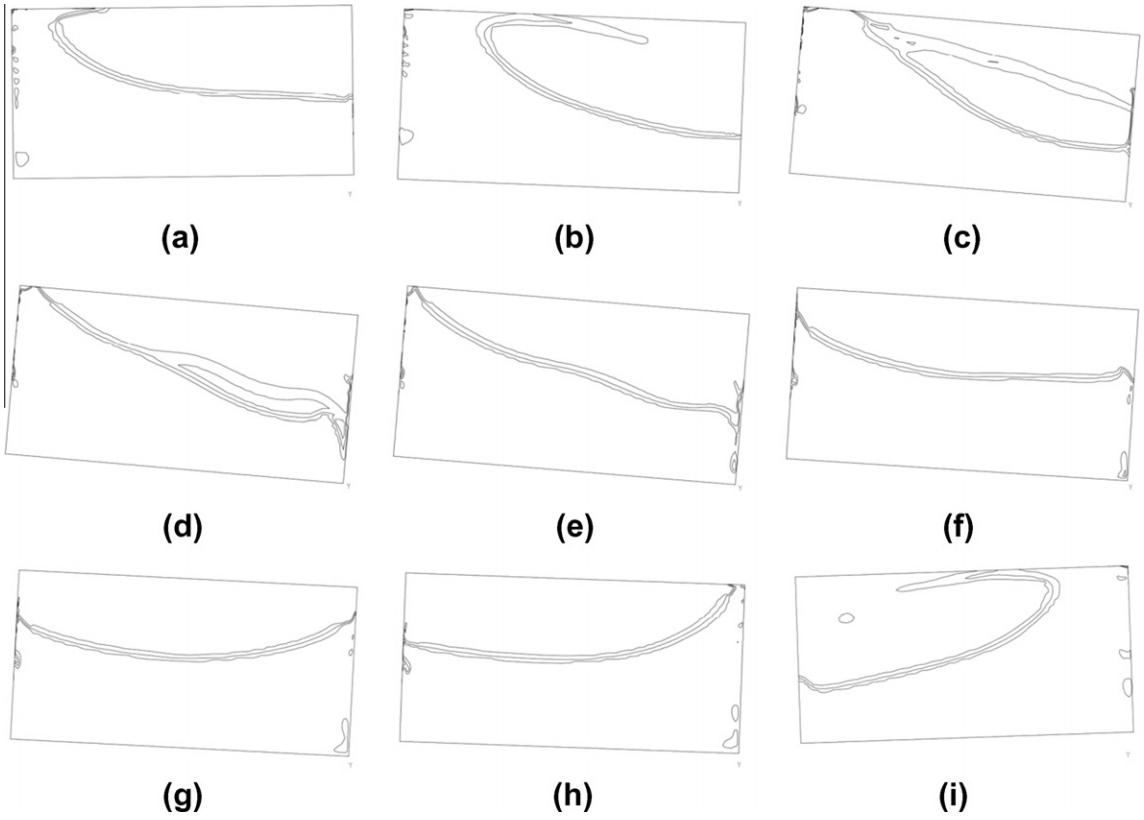

Fig. 35. Dynamic free surface location during one half oscillations for case d.

representing a typical LNG carrier membrane containment system with a filling level near the critical depth. The coefficients of the sloshing model are computed by the application of the procedure outlined in Godderidge et al. [11,12] using the results from one CFD simulation for each tank section. The initial test cases are translation and rotation – induced periodic sloshing and there is good agreement between the sloshing model and the corresponding multiphase CFD solution which is independent of the sloshing model. An arbitrary motion surge motion profile obtained from a wave spectrum describing a realistic seaway is simulated with the sloshing model and the difference to the CFD solution is approximately 6%. It is found that a conventional pendulum model is unable to emulate the sloshing response, with errors up to an order of magnitude greater than those from the Rapid Sloshing Model methodology applied in this study.

Rotational and translatory motions with identical and different frequencies are then applied simultaneously and the solutions between CFD and sloshing model continue to show good agreement. The final test is a violent sloshing flow excited by simultaneous sloshing flow and despite the limitations of the impact model the solutions remain in agreement. The advantages of pendulum sloshing model include a sufficiently low computational cost permitting simulation rates at 0.1% of real time on a desktop PC. The pendulum-based sloshing model is not restricted to a particular range of filling levels and because the fluid mass is not part of the numerical solution the resonance characteristics of the system are strictly preserved which enables simulations with large numbers of time steps. Translatory and rotational motion, or a combination thereof can be defined by either continuous functions or discrete data sets.

The properties of LNG and the increased surface roughness of some LNG containment systems can be included by changing the damping characteristics. The model can be extended to three dimensional sloshing and the impact model can be extended to include fluid structure interaction effects [18]. The current impact model is optimised for hydrodynamic impacts where the impact coincides with the maximum displacement of the fluid centre of mass but flow features observed during impact such as wave overturning and air pocket formation do not follow this assumption. Therefore, the impact model requires further improvement so that a wider range of sloshing impact physics is included.

Although a phenomenological modelling approach is based on the observation of physical behaviours of the system to be modelled and the principal features are captured in the model, the weakness of this kind of modelling approaches is the lack of explicit physical foundation for some of the details and thus empirical formulae are often adopted in the models. Hence validation is essential to establish the application areas of a particular model. Further development is needed for the Rapid Sloshing Model to predict pressure field and to account for damping due to wave breaking for low filling level sloshing cases.

The potential applications of this sloshing model include its use in a sloshing guidance system for sloshing monitoring onboard LNG carriers, a pre-screening tool for the identification of violent sloshing in a real LNG carrier motion track (typically 3 weeks duration) or incorporation in a seakeeping code for both time and frequency domain coupled sloshing-seakeeping analysis.

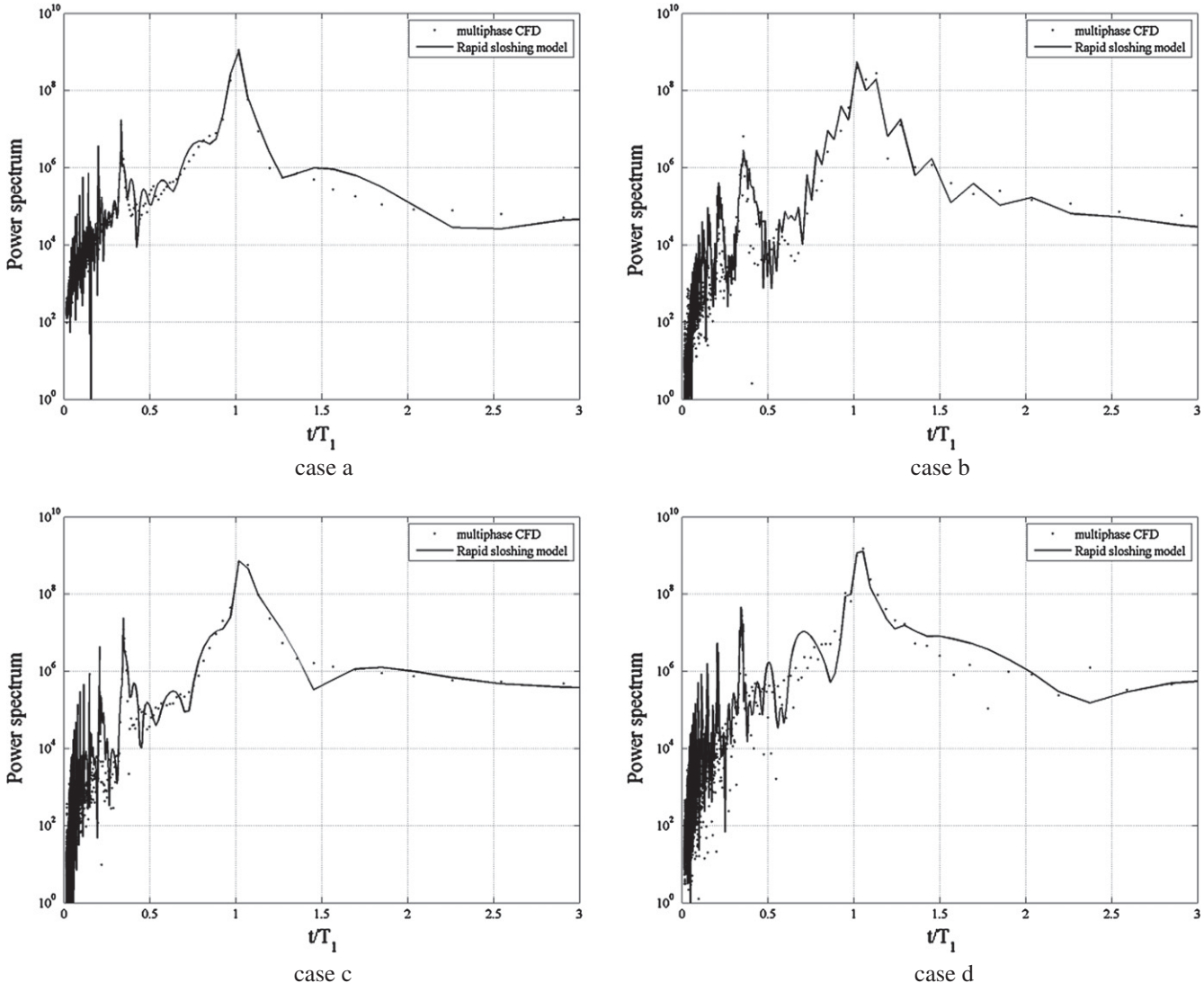

Fig. 36. Comparison of power spectra for combined surge and pitch induced sloshing.

Acknowledgements

This work was carried out under the auspices of the Engineering Doctorate Programme at the University of Southampton, with support from the Engineering and Physical Sciences Research Council (UK) and BMT SeaTech Ltd with the guidance of Nick Cowlan. The authors acknowledge the support in the scope of Project MARSTRUCT, Network of Excellence on Marine Structures financed by the European Union through the growth Programme.

References

[1] Abramson HN. The dynamic behavior of liquids in moving containers with applications to space vehicle technology. Report SP-106, National Aeronautics and Space Administration; 1966.
[2] Aliabadi S, Johnson A, Abedi J. Comparison of finite element and pendulum models for simulation of sloshing. Comput Fluids 2003;32:535–45.
[3] ANSYS Inc. CFX-11 Users Guide; 2007.
[4] Barth TJ, Jesperson DC. The design and application of upwind schemes on unstructured meshes. In: AIAA Paper 89-0366; 1989.
[5] Brennen CE. Fundamentals of multiphase flow. New York: Cambridge University Press; 2005.
[6] Dias F, Dutykh D, Ghidaglia J-M. A two-fluid model for violent aerated flows. Comput Fluids 2010;39:283–93.
[7] Dodge FT. The new dynamic behavior of liquids in moving containers. South West Research Institute, 2000. 202p.
[8] Faltinsen O. Sea loads on ships and offshore structures. Cambridge University Press; 1993.
[9] Godderidge B, Tan M, Turnock SR, Earl C. A verification and validation study of the application of computational fluid dynamics to the modelling of lateral sloshing. Ship Science Report 140, University of Southampton; 2006.
[10] Godderidge B, Tan M, Earl C, Turnock SR. Boundary layer resolution for modeling of a sloshing liquid. Intl soc offshore and polar engrs conf; 2007
[11] Godderidge B, Turnock SR, Tan M, Earl C. An investigation of multiphase CFD modelling of a lateral sloshing tank. Comput Fluids 2009;38:183–93.
[12] Godderidge B, Turnock SR, Earl C, Tan M. The effect of fluid compressibility on the simulation of sloshing impacts. Ocean Eng 2009;36(8):578–87. doi:10.1016/j.oceaneng.2009.02.004.
[13] Godderidge B, Turnock SR, Tan M. A rapid method for the simulation of sloshing using a mathematical model based on the pendulum equation. Comput Fluids 2012;57:163–71.
[14] Graczyk M, Moan T, Rognebakke O. Probabilistic analysis of characteristic pressure for LNG tanks. J Offshore Mech Arctic Eng 2006;128:133–44.
[15] Hadzic I, Mallon F, Peric M. Numerical simulation of sloshing. In: Proc of SRI-TUHH mini-workshop on numerical simulation of two-phase flows. National Maritime Research Institute & Technische Universität Hamburg-Harburg; 2001.
[16] Hinatsu M. Experiments of two-phase flows for the joint research. In: Proc of SRI-TUHH mini-workshop on numerical simulation of two-phase flows. National Maritime Research Institute & Technische Universität Hamburg-Harburg; 2001.
[17] Hine L. GTT tweaks blueprints to combat sloshing damage. LNG Unlimited, 28 November, 2008. p. 6.
[18] Ibrahim RA. Liquid sloshing dynamics. Cambridge University Press; 2005.
[19] Ishii M, Hibiki T. Thermo-fluid dynamics of two-phase flow. Springer Verlag; 2006.

[20] Lee YB, Godderidge B, Tan M, Temarel P, Turnock SR, Cowlan N. Coupling between ship motion and sloshing using potential flow analysis and rapid sloshing model. In: Proc. Intl Soc Offshore and Polar Engrs Conf; 2009.
[21] Lloyd ARJM. Seakeeping: ship behaviour in rough weather. Ellis Horwood, Chichester; 1989.
[22] Lloyds Register. Comparative sloshing analysis of LNG ship containment systems. ShipRight Additional Design Procedures; 2005.
[23] MacDonald J, Maguire J. Lloyds Register's guidance on the Operation of membrane LNG ships to avoid the risk of sloshing damage. In: 23rd Gastech conference, Bangkok; 2008.
[24] Reddy DN, Radosavljevic D. Verification of numerical methods applied to sloshing studies in membrane tanks of LNG ships. ICSOT 2006, The Royal Institution of Naval Architects; 2006.
[25] Xing JT. User manual: fluid–structure interaction analysis program-FSIAP. University of Southampton (UK): School of Engineering Sciences; 1992.
[26] Zwart PJ. Numerical modelling of free surface and cavitating flows. Industrial two-phase flow CFD: von Karman Institute Lecture Series 2004–2005, vol 25; 2004.